EMT activates ER-to-Golgi trafficking through upregulation of REEP2 to promote lung cancer progression

Kevin Fulp[1, 7], Oluwafunminiyi Obaleye[1, 7], Shike Wang[2], Xin Liu[3], Jiang Yu[3], Jonathan M. Kurie[3], Jun Xu[5], William K. Russell[6], Xiaochao Tan[2, *], Guan-Yu Xiao[1, *]

[1] Department of Toxicology and Cancer Biology, The University of Kentucky College of Medicine, Lexington, Kentucky; [2]Department of Medicine, Tulane University School of Medicine, Louisiana Cancer Research Center, New Orleans, Louisiana; [3]Department of Thoracic/Head and Neck Medical Oncology, The University of Texas MD Anderson Cancer Center, Houston, Texas; [4]Department of Molecular and Cellular Oncology, The University of Texas MD Anderson Cancer Center, Houston, Texas; [5]Department of Biochemistry and Molecular Biology, Baylor College of Medicine, Houston, Texas; [6]Department of Biochemistry and Molecular Biology, University of Texas Medical Branch, Galveston, Texas. [7]These authors contributed equally: Kevin Fulp, Oluwafunminiyi Obaleye.

*To whom correspondence should be addressed: Xiaochao Tan, Department of Medicine, Tulane University School of Medicine, New Orleans, LA 70112, USA; email: xtan4@tulane.edu; Guan-Yu Xiao, Department of Toxicology and Cancer Biology, University of Kentucky, Lexington, KY 40508, USA. Email: guan-yu.xiao@uky.edu.

Abstract

Membrane trafficking governs the transport of molecules to both intracellular and extracellular locations, thereby maintaining cell homeostasis. During cancer progression, alterations in membrane trafficking are frequently observed. However, the mechanisms underlying the dysregulation of membrane trafficking in cancer progression remain largely unresolved. Recent

evidence has demonstrated that epithelial-to-mesenchymal transition (EMT) in lung adenocarcinoma (LUAD) employs a membrane trafficking program to coordinate cancer cell invasion and immunosuppression in the tumor microenvironment (TME). To further dissect the pro-tumorigenic membrane trafficking program, here we conducted a CRISPR interference (CRISPRi) *in vivo* screen for membrane trafficking regulators in a syngeneic mouse model with a complete immune system. This screen identified REEP2, an endoplasmic reticulum (ER) shaping protein, as a novel regulator of the EMT-dependent membrane trafficking program, which is associated with a poor prognosis in LUAD patients and is required for LUAD metastasis in a syngeneic orthotopic LUAD mouse model. Mechanistically, the EMT activator ZEB1 upregulates REEP2 expression through miR-183- and miR-193a-mediated regulation that promotes the transportation of secretory cargoes from the ER exit site (ERES) to the Golgi, thereby augmenting the secretion of pro-tumorigenic factors. The REEP2-driven secretion promotes cancer cell proliferation, migration, and the infiltration of myeloid-derived suppressor cells (MDSCs) in the TME. These findings identify REEP2 as a critical mediator of the EMT-driven pro-metastatic membrane trafficking program, revealing a specific vulnerability in mesenchymal LUAD.

Introduction

Membrane trafficking, a highly regulated process that is essential for cellular homeostasis, is disrupted on multiple levels in cancer, framing a new frontier in targeted therapeutics for cancer treatments (Elkin et al., 2016; Ferreira et al., 2024; Huang et al., 2019; Makaraci and Kim, 2018; Maxfield and McGraw, 2004; Tan et al., 2024; Tejeda-Munoz et al., 2022). It involves the complex coordination of a host of vesicles shuttling an array of cargo to and from the endoplasmic reticulum (ER), Golgi apparatus, the plasma membrane, and extracellular space (Di Martino et al., 2019; Elkin et al., 2016; Makaraci and Kim, 2018; Maxfield and McGraw, 2004). Numerous cancer-associated mutations have been identified in the components of the membrane trafficking machinery (Lanzetti and Di Fiore, 2008; Mosesson et al., 2008). Furthermore, cancer cells

53 coordinate membrane trafficking components post-transcriptionally (i.e. microRNA regulation)
54 (Banerjee et al., 2021; Tan et al., 2021; Tan et al., 2023; Xiao et al., 2023) and post-translationally
55 (i.e. phosphorylation) (Chen et al., 2017; Lakoduk et al., 2019; Reis et al., 2015; Schmid, 2017;
56 Xiao et al., 2018; Xiao and Schmid, 2020) to dynamically adapt membrane trafficking pathways
57 and acquire metastatic capabilities. Although numerous genome-wide analyses have been
58 performed to interrogate the roles of membrane trafficking components in cancer cells (Liberali et
59 al., 2014; Pelkmans et al., 2005), many critical knowledge gaps remain regarding the mechanisms
60 of their dysregulation in cancer progression, and this area continues to be fertile ground for the
61 discovery of novel cancer treatments.

62 Recent studies reveal that epithelial-to-mesenchymal (EMT)-activating transcription factors
63 coordinate membrane trafficking networks to establish a front-rear polarity axis that facilitates
64 cancer cell motility (Banerjee et al., 2021; Corallino et al., 2015). Importantly, the EMT-driven
65 membrane trafficking program underlies a vulnerability of EMT-driven metastatic cancers (Tan et
66 al., 2023; Xiao et al., 2023), and the inhibition of EMT-activated membrane trafficking regulators
67 reactivates anti-tumor immunity in the tumor microenvironment (TME) and reverses acquired
68 resistance to immune checkpoint inhibitor (ICI) therapy in LUAD (Xiao et al., 2023). However, no
69 comprehensive studies have systematically examined how membrane trafficking machinery
70 influences TME that is essential for cancer progression.

71 To identify the membrane trafficking regulators critical for tumor growth with immune selective
72 pressure, here we conducted a CRISPR repression (CRISPRi) *in vivo* screen in a syngeneic
73 mouse model. Using LUAD cell lines derived from humans and genetically engineered mice that
74 develop metastatic LUAD, which are classified as epithelial or mesenchymal (Ahn et al., 2012;
75 Gibbons et al., 2009; Tan et al., 2017; Xiao et al., 2023) (Table S1), we further investigated
76 regulatory mechanisms of the identified candidate, REEP2, an endoplasmic reticulum (ER)
77 shaping protein, in membrane trafficking and LUAD progression. The findings presented herein
78 uncover a molecular underpinning by which EMT promotes the secretory cargo transportation

79 from the ER exit site (ERES) to the Golgi and, in turn, enhances the secretion of pro-tumorigenic
80 factors that foster cancer cell motility and immunosuppressive TME.
81
82 **Results**
83 **Pro-tumorigenic membrane trafficking program for LUAD growth**
84 To systematically characterize the EMT-driven membrane trafficking in LUAD progression and
85 immunosuppression, we transduced a CRISPR interference (CRISPRi) library targeting 2,099
86 trafficking-related genes (Horlbeck et al., 2016) into murine mesenchymal LUAD 344SQ cells,
87 which develop into metastatic LUADs owing to high expression of the EMT activator, ZEB1
88 (Gibbons et al., 2009) (Fig. 1A). We performed an *in vivo* screen by transplanting the cells into
89 syngeneic wild-type (WT) immunocompetent mouse flanks and measured the effects on
90 tumorigenesis (Fig. 1A). This screen revealed a panel of membrane trafficking regulators required
91 for tumor growth under immune surveillance (fold-change ($\log_2$) < -1, FDR ($-\log_{10}$) > 20) (Fig. 1B,
92 blue box, Table S2). We prioritized a set of top hits (fold-change ($\log_2$) < -2 and FDR ($-\log_{10}$) > 20,
93 Fig. 1B, red dots and Fig. 1C) and assessed their correlation with EMT (Fig. 1D) and prognostic
94 values (Fig. 1E and Fig. S1) using The Cancer Genome Atlas (TCGA) database. We identified
95 several membrane trafficking regulators (*KRT16, REEP2, TNNT1, ARL14*) that significantly
96 correlate with the EMT signature and shorter survival durations of LUAD patients. These findings
97 reveal a membrane trafficking program that contributes to LUAD tumorigenesis. Among these hits,
98 REEP2 represents the strongest EMT correlation and demonstrates high prognostic value, and
99 correlates with LUAD metastasis (Fig. 1F).
100
101 **REEP2 is required for mesenchymal LUAD metastasis**
102 To further investigate the function of REEP2 in LUAD progression, we subjected murine
103 mesenchymal 344SQ cells to CRISPR/Cas9-mediated REEP2 knockout (REEP2 KO) (Fig. S2A),
104 and inoculated the cells orthotopically in the lungs of the syngeneic WT mice. We found that

105 REEP2 KO cells generated orthotopic LUADs that were smaller (Fig. 2A, left dot plot) and less
106 metastatic to the mediastinum (Fig. 2A, middle dot plot) and the contralateral lung (Fig. 2A, right
107 dot plot). We then assessed cancer progression properties *in vitro* and found that REEP2
108 depletion (Fig. S2A-D) reduced murine (344SQ) and human (H1299) mesenchymal LUAD cell
109 proliferation (Fig. 2B), but negligibly affected the viability of human epithelial LUAD (HCC827) (Fig.
110 S2E) or non-cancerous human bronchial epithelial cell (HBEC30KT) (Fig. S2F). Furthermore, we
111 found that REEP2 deficiency in mesenchymal LUAD cells resulted in cell cycle arrest (Fig. 2C),
112 with a negligible change in apoptosis (Fig. 2D), and sharply reduced migratory and invasive
113 activities in Boyden chambers (Fig. 2E and F). These data indicate a significant, previously
114 unknown association of REEP2 with LUAD progression.
115
116 **ZEB1 relieves REEP2 from microRNA-dependent silencing**
117 We identified a positive correlation between ZEB1 and REEP2 expressions in human LUAD
118 (Fig. 3A) and validated that their mRNA and protein levels changed in a corresponding fashion
119 following ZEB1 gain- or loss-of-function (Fig. 3B, S3A). ZEB1 has been shown to silence
120 microRNAs (miRs) to relieve the negative transcriptional regulation from genes involved in LUAD
121 progression (Ahn et al., 2012; Banerjee et al., 2021; Tan et al., 2017; Xiao et al., 2023). Using the
122 TargetScan prediction tool (www.targetscan.org), we identified predicted miR-183 and miR-193a
123 binding sites on the REEP2 3'-untranslated regions (3'-UTRs) (Fig. S3B). In the epithelial cells
124 with inducible ZEB1 expression (H322_iZEB1), ZEB1 induction repressed the expressions of both
125 miR-183 and miR-193a, while upregulating REEP2 simultaneously (Fig. S3C). We found that
126 miR-183 and miR-193a mimics reduce REEP2 expression in murine and human mesenchymal
127 LUAD cells (Fig. 3C, S3D). To validate the miR-183- and miR-193a-mediated REEP2 silencing,
128 we mutated the predicted binding sites (Fig. S3B) and found that both miR-183 and miR-193a
129 mimics suppressed the activity of human REEP2 reporters containing wild-type but not mutant 3'-
130 UTRs lacking predicted binding sites (Fig. 3D and E). These findings define a REEP2 regulatory

131 axis in which ZEB1 alleviates miRNA-mediated repression, leading to REEP2 upregulation in
132 mesenchymal LUAD.
133
134 **ZEB1 coordinates REEP2 to promote ERES and Golgi colocalization in mesenchymal**
135 **LUAD**
136 REEP proteins are known to generate membrane curvature of the ER to regulate its structure
137 and function (Fan et al., 2022) and have been suggested to function in secretory trafficking (Hurt
138 et al., 2014). Proteins destined for secretion are synthesized in the ER, where cargoes are
139 packaged into ERES and transferred to the Golgi apparatus (Weigel et al., 2021), after which they
140 are directed to the plasma membrane through post-Golgi traffic (Szul and Sztul, 2011). SEC
141 proteins, including SEC16 and SEC24, are recruited to the site of ERES and are essential for the
142 formation of ERES and cargo packaging (Hughes et al., 2009; Robinson et al., 2024; Sprangers
143 and Rabouille, 2015). GM130 at the cis-Golgi tethers ERES cargo delivery to the Golgi (Linstedt
144 et al., 2000). Given the significant curvature at the ERES, we hypothesized that ZEB1 coordinates
145 REEP2 to direct ERES toward the Golgi in mesenchymal LUAD (Fig. 4A). To test the possibility,
146 we visualized the distribution of SEC16A and GM130 using immunofluorescence. Strikingly,
147 compared to empty vector control (Vec), which showed the dispersed SEC16A signals outside of
148 the Golgi area marked by GM130 (Fig. S4A, arrows), ectopic ZEB1 expression remarkably
149 increased SEC16A colocalization with GM130 (Fig. S4A, arrowheads) in the epithelial murine
150 (393P) LUAD cells. The depletion of ZEB1 in the mesenchymal murine (344SQ) and human
151 (H1299) LUAD cells reduced the SEC16A/GM130 colocalization (Fig. S4B and C). The deficiency
152 of REEP2 similarly decreased their colocalization in the mesenchymal human (H1299) LUAD
153 cells (Fig. S4C). Furthermore, the ectopic expression of ZEB1 in the epithelial human (HCC827)
154 LUAD cells increased the SEC16A/GM130 colocalization (Fig. 4B, Vec vs. siCTL), while REEP2
155 depletion (Fig. S4D) abolished the phenotype (Fig. 4B, siCTL vs. siREEP2s). We then observed
156 the consistent findings of higher colocalization between SEC24D-labelled ERES and the Golgi in

157 the epithelial human (HCC827) LUAD cells with ectopic ZEB1 expression compared to Vec (Fig.
158 4C), while REEP2 depletion disrupted the phenotype (Fig. 4D), suggesting ZEB1 coordinates
159 REEP2 to promote ERES locating on the Golgi in mesenchymal LUAD.

160 Thus far, REEP2 was observed to form vesicular structures that lack colocalization with
161 markers of canonical cellular compartments (Shibata et al., 2024). To further investigate the
162 distribution and function of REEP2, we transfected the HCC827 cells with fluorescent-tagged
163 REEP2 (Fig. S4E) and found that the REEP2 vesicles highly colocalized with SEC24D-labelled
164 ERES (~80%) and there was no difference between ectopic Vec and ZEB1 expression (Fig. S4F).
165 However, the ectopic expression of ZEB1 significantly enhanced the ERES colocalization with the
166 Golgi (Fig. 4E). Strikingly, we observed that the SEC24D structures with REEP2 coating
167 dramatically increased their colocalization with the Golgi, compared to those lacking REEP2
168 coating, and ectopic ZEB1 expression further raised the colocalization (Fig. 4F). These findings
169 suggest that REEP2 recruitment to the ERES is necessary for their transportation to the Golgi.

170

171 **REEP2-driven ERES/Golgi colocalization promotes secretory trafficking**

172 To test how REEP2-driven ERES/Golgi colocalization influences protein trafficking, we used
173 the retention using selective hooks (RUSH) system (Boncompain et al., 2012) to quantitatively
174 monitor trafficking kinetics at different time points. Human mesenchymal LUAD cells (H1299)
175 were transfected with a GFP-tagged CD-MPR, a canonical cargo that localizes to the trans-Golgi
176 network (TGN) (Waguri et al., 2003), which binds to streptavidin fusing with an ER retention signal
177 (Lys-Asp-Glu-Leu; KDEL) via the streptavidin-binding peptide (SBP) (Fig. S5A). Upon biotin
178 treatment, the CD-MPR-RUSH is released from the ER and trafficked to the Golgi (Fig. 5A, siCTL,
179 S5A). REEP2 depletion drastically reduced the trafficking of CD-MPR-RUSH to the Golgi at both
180 10 minutes and 30 minutes post-Biotin treatment (Fig. 5A).

181 Next, to assess whether ERES/Golgi colocalization facilitates secretory trafficking, the ER
182 stress inducer, thapsigargin, was used to disperse SEC16A (Hughes et al., 2009), and the

183 temperature-sensitive mutant vesicular stomatitis virus (VSV-G) assay was used to measure
184 secretory trafficking (Fig. S5B). Consistent with the previous study (Hughes et al., 2009),
185 thapsigargin disrupted ERES colocalization with the Golgi (Fig. S5C). We observed that the
186 reduced ERES/Golgi colocalization impacted secretory trafficking in the mesenchymal human
187 (H1299) LUAD cells (Fig. S5D). We found that ZEB1 promoted secretory trafficking in the
188 epithelial human (HCC827) LUAD cells and that the depletion of REEP2 abated the phenotype
189 (Fig. 5B). These findings suggest that REEP2 coordinates ERES/Golgi colocalization to promote
190 secretory trafficking.
191
192 **REEP2 regulates the secretion of pro-tumorigenic factors**
193 Given that REEP2 promotes secretory trafficking, we hypothesized that REEP2 facilitates the
194 secretion of pro-metastatic factors in mesenchymal LUAD cells. To test this, we evaluated
195 whether REEP2-dependent secretions could modulate epithelial LUAD cell behaviors in a
196 paracrine manner. Conditioned medium (CM) from REEP2-replete HCC827_ZEB1 cells induced
197 a decrease in the G_0/G_1 population and a corresponding increase in S-phase of HCC827_Vec
198 cells (Fig. 6A), and enhanced the cell mobility (Fig. 6B), whereas CM from REEP2-deficient
199 HCC827_ZEB1 cells demonstrated no effects (Fig. 6A and B). These findings suggest that the
200 REEP2-driven secretome contributes to the metastatic properties of LUAD cells.
201 To explore REEP2-dependent secreted factors, we performed liquid chromatography-mass
202 spectrometry (LC-MS) analysis on CM collected from REEP2-replete HCC827_ZEB1 cells, and
203 their REEP2-depleted counterparts. We found that REEP2 depletion reduced secretion of factors
204 involved in the immunomodulatory and cell migratory pathways (Fig. S6A, blue and red dots)
205 (Dataset S1), defined by enrichment analysis (Fisher's exact test using Gene Ontology terms) of
206 the down-regulated secreted proteins (Fig. S6B), including autotaxin (ATX). We have recently
207 identified ATX as a predominant secretory factor in the EMT-driven secretion that promotes LUAD
208 cell motility in autocrine and paracrine mechanisms and mediates the immunosuppressive TME

209 (Xiao et al., 2023). Enzyme-linked immunosorbent assays (ELISA) on CM samples confirmed that
210 REEP2 depletion reduces the secretion of ATX (Fig. S6C), whereas the intracellular ATX remains
211 unchanged (Fig. S6D).

212 Given that we identified numerous immunomodulatory proteins that were diminished by
213 REEP2 depletion (Fig. S6A, red dots), we speculate that REEP2-regulated secretome remodels
214 TME. We used TIMER2.0 (Li et al., 2016; Li et al., 2017; Li et al., 2020) to analyze the immune
215 infiltrates in human LUAD cataloged in TCGA. We found that high REEP2 expression positively
216 correlates with higher infiltration levels of myeloid-derived suppressor cells (MDSCs) and
217 regulatory T cells (Tregs) in human LUAD (Fig. 6C and D). Therefore, we reasoned that REEP2
218 may create an immunosuppressive TME and addressed this possibility by carrying out flow
219 cytometry on flank tumors generated by REEP2-replete or -deficient murine LUAD cells in
220 syngeneic, immunocompetent mice. We found that REEP2 depletion enhanced total $CD8^+$ T cells
221 but reduced naïve $CD8^+$ T cells and MDSCs (Fig. 6E) in the TME, and suppressed tumor growth
222 (Fig. 6F). These findings suggest that REEP2 promotes the secretion of pro-tumorigenic factors
223 required for LUAD progression.

224

225 **Discussion**

226 Growing evidence shows that alterations in membrane trafficking frequently occur during
227 cancer progression and, in turn, promote metastasis (Evergren et al., 2024), indicating significant
228 therapeutic potential for these pathways. Here, we show that EMT initiates a membrane trafficking
229 program essential for LUAD tumorigenesis under immunosurveillance and identify that ZEB1
230 coordinates REEP2 via miR-183/miR-193a to enhance ERES colocalization with the Golgi,
231 thereby facilitating the secretion of pro-metastatic factors that promote LUAD metastasis (Fig. 6G).
232 This regulatory axis discloses a potential therapeutic vulnerability in EMT-driven metastatic
233 cancers.

234 The REEP family comprises six ER-localized membrane-shaping proteins that facilitate high
235 membrane curvature. REEP1-4 share structural motifs and are less abundant than REEP5 and
236 6, which are more broadly expressed (Fan et al., 2022). Germline mutations in REEP1 and
237 REEP2 cause hereditary spastic paraplegia (HSP) and related motor neuropathies (Esteves et
238 al., 2014; Zuchner et al., 2006), underscoring their physiological importance in ER shaping and
239 neuronal maintenance. Additionally, REEP family members have been implicated in tumor biology.
240 REEP4 is upregulated in renal carcinoma, where its expression aligns with tumor aggressiveness
241 (Chen et al., 2024), and REEP6 expression correlates with poor prognosis in oral squamous cell
242 carcinoma (Tseng et al., 2023). Moreover, REEP5 and REEP6 have been shown to potentiate
243 CXCR1/IL-8 signaling and promote proliferation and metastasis in lung cancer cells (Park et al.,
244 2016). These findings suggest that REEP family proteins broadly contribute to tumor progression,
245 though their mechanisms and context-specific roles are still elusive. Here, we show for the first
246 time that REEP2 is a downstream effector of ZEB1-dependent transcription program that
247 activates ER-to-Golgi trafficking of secretory cargoes required for EMT-driven metastasis in LUAD.
248 A recent study demonstrated that REEP1-4 form a distinct ER-derived vesicular compartment
249 and regulate ER tubule dynamics (Esteves et al., 2014; Zuchner et al., 2006), but their roles in
250 membrane trafficking remain largely unexplored. Here, we demonstrate that REEP2 is recruited
251 to ERES, where it locates ERES on the Golgi and, in turn, promotes secretory trafficking.
252 Interestingly, although ectopic REEP2 expression is sufficient to drive ERES/Golgi colocalization
253 in epithelial cells (Fig. 4E vs. Fig. 4C, HCC827_Vec), REEP2 enhances the colocalization in a
254 ZEB1-dependent manner (Fig. 4E). Whether this occurs via direct interactions between REEP2
255 and its interactors, which are co-opted by ZEB1, or indirectly through other altered membrane
256 trafficking regulators in mesenchymal cells warrants to be determined.
257 Here, we identified a set of REEP2-dependent secreted proteins. ATX is aberrantly secreted
258 by many human cancers to enhance cancer cell motility through lysophosphatidic acid receptors
259 (LPARs) (Aiello and Casiraghi, 2021; Kato et al., 2012; Liu et al., 2009; Yu et al., 2008). Our

260 recent study has shown that ATX is a key secretory effector within the EMT-driven secretome,
261 contributing to cell motility (Xiao et al., 2023). Furthermore, the ATX-CXCL1 axis recruits MDSCs
262 while inhibiting cytotoxic $CD8^+$ T-cell infiltration (Pietrobono et al., 2024) and interleukin (IL)-6, a
263 crucial regulator of MDSC accumulation and activation (Weber et al., 2021). REEP2 depletion
264 suppresses the secretion of these factors. These findings are consistent with clinical data and our
265 mouse model, however, it remains to be determined whether the REEP2-driven secretory
266 program relates to LUAD progression and metastasis and how it correlates to EMT and the
267 immune landscape of the TME in LUAD patients.
268 In summary, our findings reveal REEP2 as a previously unrecognized effector of EMT-driven
269 membrane trafficking program in LUAD, highlighting that REEP2-mediated ERES-Golgi coupling
270 underlies the EMT-driven hypersecretory state.
271
272
273
274
275

276 **Methods**

277 Animal husbandry

278 For CRISPRi *in vivo* screen, all mouse studies were approved by the Institutional Animal Care
279 and Use Committee at The University of Texas MD Anderson Cancer Center (Houston, Texas).
280 Mice underwent standard care and were killed at predetermined time points or at first signs of
281 morbidity according to the standards set forth by the Institutional Animal Care and Use Committee.
282 To generate subcutaneous tumors, we injected 344SQ cells (1.1×10^6 cells in 100 μL PBS) into
283 the right flanks of syngeneic, immunocompetent 129-Elite (SOPF) mice (#476, Charles River
284 Laboratories) (n = 6 per cohort). Tumor volumes were monitored weekly until tumors reached
285 maximum size (~2 cm^3 total volume per mouse), and then the mice were sacrificed and the tumors
286 were harvested, as previously described (Martin et al., 2021).

287 All other mouse studies were approved by the Institutional Animal Care and Use Committee
288 at The University of Kentucky (Lexington, Kentucky). Mice underwent standard care and were
289 killed at predetermined time points or at first signs of morbidity according to the standards set
290 forth by the Institutional Animal Care and Use Committee. To generate orthotopic lung tumors,
291 we intrathoracically injected 344SQ cells (0.5×10^6 cells in 50 μL PBS) phosphate-buffered saline
292 into the left lungs of syngeneic, immunocompetent 129-Elite (SOPF) mice (n = 10 per cohort) and
293 carried out necropsies 14 d later to quantify primary tumor size and metastases to mediastinal
294 lymph nodes and contralateral lung as we previously described (Xiao et al., 2023). To generate
295 subcutaneous tumors, we injected 344SQ cells (0.5×10^6 cells in 100 μL PBS) into the right flanks
296 of syngeneic, immunocompetent 129-Elite (SOPF) mice (n = 10 per cohort). Tumor volumes were
297 measured weekly, and mice were sacrificed at 5 weeks post-injection, and necropsy was
298 performed to quantify primary tumor weights and assess the presence of pleural surface lung
299 metastases, as previously described (Xiao et al., 2023).

300

301 CRISPRi screens

302 The CRISPRi library virus preparation and screen were performed as previously described (Martin
303 et al., 2021). In brief, a library of gRNAs targeting 2,099 known or putatively membrane trafficking
304 genes with 5 gRNAs per gene for a total of 11,040 gRNAs (#83992, Addgene) (Horlbeck et al.,
305 2016) in the pCRISPRia-v2 vector (#84832, Addgene), and KRAB-dCas9-mCherry (#60954,
306 Addgene), along with the psPax2 (Addgene cat# 12260) and pMD2.G (Addgene cat# 12259)
307 lentiviral packaging vectors, were transfected into 293T cells for virus production by The
308 Functional Genomics Core (The University of Texas MD Anderson Cancer Center, Houston,
309 Texas). CRISPR library virus was used to titer on the murine mesenchymal LUAD 344SQ cells.
310 The amount of virus that resulted in ~30% cell positivity following cell sorting selection based on
311 the BFP signal in the pCRISPRia-v2 vector was scaled up for library infection to ensure low
312 multiplicity of infection (0.3) and appropriate library representation (500X for each sgRNA) after
313 selection. Cells were infected in triplicate to generate biological replicates by The Functional
314 Genomics Core.
315 On the day of animal injection, an initial time point (T0) of infected cells was harvested to
316 determine a baseline of sgRNA abundance. For *in vivo* CRISPRi screens, three independent
317 infections with the CRISPR library composed of biological replicates in the screening experiments.
318 Each replicate was inoculated into the right flanks of 6 different 6-8-week-old 129-Elite (SOPF)
319 mice with 1.1 million cells per injection. The tumors were harvested when they reached ~2 cm^3
320 total volume. The T0 infected cells and tumors were digested and the genomic DNA was extracted
321 by The Biospecimen Extraction Facility (The University of Texas MD Anderson Cancer Center,
322 Houston, Texas). The next-generation sequencing of sgRNA and analysis of sgRNA abundance
323 were performed by VectorBuilder Inc. (Chicago, Illinois).
324
325 Reagents
326 We purchased fetal bovine serum (FBS), live-cell imaging solution, phosphate-buffered saline
327 (PBS), RPMI-1640, Trypsin-EDTA (0.25%), Alexa Fluor-tagged secondary antibodies,

328 paraformaldehyde, bovine serum albumin (BSA), DAPI and Triton X-100, High-Capacity cDNA
329 Reverse Transcription Kit, PowerUp™ SYBR™ Green Master Mix, and protease/phosphatase
330 inhibitor cocktail from Thermo Fisher Scientific; Doxycycline (#D9891) from MilliporeSigma;
331 Bronchial Epithelial Cell Growth Medium BulletKit from Lonza; jetPRIME transfection reagent from
332 Polyplus Transfection; Transwell and Matrigel-coated Boyden chambers from BD Biosciences;
333 Glass-bottom dishes and multiwell plates from MatTek; 10X Cell lysis buffer from Cell Signaling
334 Technologies; 2X cell lysis buffer (#1610737) from Bio-Rad; CCK-8 (#K1018) from APExBIO;
335 RNeasy Plus Mini Kit (#74136), and AllStars Negative Control siRNA (#1027281) from QIAGEN;
336 Pre-miR™ miRNA Precursor Negative Control (miR-NC) (#AM17110); human miR-183a mimics
337 (#PM12303) and human miR-193 mimics (#PM11786) from Thermo Fisher Scientific; human
338 REEP2 siRNA #2 (#J-021201-18), and #4 (J-021201-20) from Horizon; primary antibodies against
339 β-actin (#4967), ZEB1 (#3396) from Cell Signaling Technologies, REEP2 (#Ab191410) from
340 Abcam, SEC16A (#20025-1-AP) from Proteintech, VSV-G (#EB0012) from Kerafast; Alexa Fluor
341 555 Mouse anti-GM130 (#560066) from BD Biosciences; REEP2-GFP (#RC202507L4) from
342 Origene; SEC24D-mCherry (#32677), Golgi-pmTurquoise2 (#36205), mCherry-Golgi (#55052)
343 and CD-MPR-GFP-RUSH (#202797) from Addgene; 3'-UTR luciferase reporters of REEP2
344 (#38786081) from Applied Biological Materials; pCI-Neo Renilla luciferase reporter (Basic)
345 (#E1841) and pGL3 Basic Firefly luciferase control reporter (#E1751) from Promega; All-in-One
346 miRNA qRT-PCR Detection Kit 2.0 (#QP115) from GeneCopoeia.
347
348 Cell lines and culture
349 Murine LUAD cell lines were derived previously (Gibbons et al., 2009). Human LUAD cell lines
350 were from Jonathan Kurie (The University of Texas MD Anderson Cancer Center, Houston,
351 Texas). Human HBEC30KT cell line was from John Minna (The University of Texas Southwestern
352 Medical Center, Dallas, Texas). Murine and human LUAD cell lines were cultured in RPMI-1640
353 with 10% FBS. Human HBEC30KT cell line was cultured in Bronchial Epithelial Cell Growth

354 Medium BulletKit. Cells were maintained at 37°C in an incubator with a humidified atmosphere
355 containing 5% CO2. Cells were transfected with vectors using jetPRIME transfection reagent.
356
357 CRISPR/Cas9
358 CRISPR-Cas9-mediated murine REEP2 Knockout 344SQ cells were generated in the Cell-Based
359 Assay Screening Service Core Facility (Baylor College of Medicine) using the following guide
360 RNA sequences: 5′-aaagaugagccuagggaagc-3' and 5′-aaacagaugggaguagagug-3'.
361
362 Live and fixed cell imaging
363 Cells were seeded on type I collagen-coated cover glass (#1.5). Live cells were imaged in live-
364 cell imaging media within incubation chambers. For fixed-cell imaging, cells were fixed using 4%
365 paraformaldehyde for 10 min, permeabilized using 0.1% Triton X-100 for 5 min, and blocked with
366 5% BSA for 1h. Primary antibody incubation was performed in blocking buffer for 1 h overnight at
367 4°C, followed by Alexa Fluor-conjugated secondary antibodies in blocking buffer for 1 h at room
368 temperature. Nuclei were counterstained with DAPI (#R37606, Thermo Fisher Scientific), and a
369 cover glass was mounted using ProLong Diamond Antifade Mountant (#P36970, Thermo Fisher
370 Scientific). Each step was followed by washing 3 times with PBS, which was also used as the
371 solvent in all steps. For VSV-G assay, the cells were not permeabilized.
372
373 VSV-G assay
374 The VSV-G transport assay was performed as described previously (Xiao et al., 2023). In brief,
375 cells were transiently transfected with EGFP-VSV-G (ts045), transferred to the restrictive
376 temperature of 40°C for 20 h, and then transferred to the permissive temperature of 32°C for 1 h
377 in the presence of 100 mg/ml cycloheximide, at which point the cells were fixed. In
378 nonpermeabilized cells, exofacial and total VSV-G were detected by staining with an anti–VSV-G
379 antibody and by measurement of EGFP signal intensity, respectively. VSV-G trafficking to the

380 plasma membrane was measured based on the ratio of exofacial (surface) VSV-G fluorescence
381 signal to the EGFP (total) signal intensity.
382
383 RUSH assay
384 The RUSH assay was performed as described previously (Boncompain et al., 2012; Boncompain
385 and Perez, 2012). In brief, cells were transiently transfected with a CD-MPR reporter, which is
386 fused to the streptavidin-binding peptide (SBP), GFP-tag, and a second protein with a C-terminal
387 ER retention signal (Lys-Asp-Glu-Leu; KDEL) fusing with streptavidin as a hook (#202797,
388 Addgene). mCherry-Golgi (#55052, Addgene) was transiently co-transfected to label the Golgi
389 compartment. BioLock (#2-0205-050, IBA Life Sciences) was used to quench excessive biotin in
390 the culture medium according to manufacturer's instructions. Twenty hours after transfection, the
391 release of the RUSH cargos was induced by addition of 40 μM of D-biotin (#B4501,
392 MilliporeSigma). Time-lapse acquisitions were done at 37 °C in a thermostat-controlled Nikon
393 stage top incubator (Nikon Instruments).
394
395 Microscopy
396 Fixed and live-cell imaging were performed on Nikon CSU-W1 SoRa Confocal Microscope (Nikon
397 Instruments) equipped with 60X/1.4 NA Oil, 100X/1.45 NA Oil objectives; 405/488/561/647 nm
398 laser lines; GaAsP detectors, and Nikon stage top incubator. Images were acquired using NIS-
399 Elements software (Nikon instruments).
400
401 Image processing and quantitative analysis
402 For fixed cell imaging, the raw images were processed, and fluorescent intensity was analyzed in
403 Fiji/ImageJ (www.imagej.nih.gov). For live cell imaging, the raw images were processed/analyzed
404 in Imaris 10.0.1 (Bitplane software, Oxford instruments) with Spot features and MATLAB
405 XTensions.

406

407 Quantitative RT-PCR

408 Total RNA was isolated from cells using RNeasy Plus Mini Kit and subjected to reverse
409 transcription and qPCR analysis as described (Tan et al., 2018). mRNA levels were normalized
410 based on ribosomal protein L32 (RPL32) mRNA. MicroRNA levels were detected using the All-in-
411 One miRNA qRT-PCR Detection Kit 2.0 with a universal reverse primer (#QP115, GeneCopoeia)
412 according to the manufacturer's instructions and normalized to U6. Primer sequences are listed
413 in Table S3.

414

415 Luciferase reporter assays

416 For 3′-UTR activity assays, H1299 cells were co-transfected with luciferase reporters driven by
417 REEP2-3'-UTR sequences (100 ng) or pCI-Neo Renilla luciferase reporter (Basic) (100 ng), pGL3
418 Basic Firefly luciferase control reporter (100 ng), and microRNA mimics or control mimics (20 μM).
419 After 48 hours, firefly and Renilla luciferase activities were measured with the Dual-Luciferase
420 Reporter Assay System (Promega).

421

422 Mutagenesis

423 Q5 Site-Directed Mutagenesis Kit (#E0554S, NEB) was used to generate mutants according to
424 the manufacturer's instructions. The primer sequences utilized for mutagenesis are: 5'-
425 TCATTGGGTGGGGCTGAAAAAAACATGTTCCCACATTAAAA-3' and 5'-
426 CAGCCCCACCCAATGACCAGGAAAAGAG-3' for human REEP2 3'UTR MT1 (miR-183 binding
427 stie); 5′-AAAGAGGCCCCTCCTGAGGCTTCA-3′ and 5′-TTTAGCCCCTGCTCCACACTGTGC-3′
428 for human REEP2 3'UTR MT2 (miR-193a binding stie 1); 5′-
429 AAATAGGGCCCAGTCTGCTTGGTACAG-3′ and 5′-TTTTCTGGCAGAACCCAGCCTCTG-3′ for
430 human REEP2 3'UTR MT3 (miR-193a binding stie 2). All primers were purchased from Integrated
431 DNA Technologies.

432

433 Western blotting

434 Cells cultured in each well of a 6-well plate at 80% confluency were washed three times with PBS
435 and harvested/resuspended in 150–200 μl of 2× Laemmli buffer (Bio-Rad). The cell lysate was
436 boiled for 10 min and loaded onto an SDS gel. After transferring to a nitrocellulose membrane
437 (Bio-Rad), membranes were blocked with 5% milk in TBST buffer and were probed with primary
438 antibodies diluted in 5% BSA in TBST buffer. Horseradish peroxidase (HRP)-conjugated
439 secondary antibodies were used according to the manufacturers' instructions. Quantitative
440 analysis was performed by using Fiji/ImageJ (NIH).

441

442 Cell proliferation assay

443 Cells were seeded on 96-well plates at a density of $2*10^3$ cells per well on day 0. Relative cell
444 density was measured by using the CCK-8 Counting Kit according to the manufacturer's
445 instructions. Briefly, cells were incubated with culture medium containing the CCK-8 solution for
446 2 h at 37 °C, and the absorbance was read at 450 nm.

447

448 Cell cycle assay

449 Cells were synchronized using culture medium containing 0.1% FBS for 24 h, then allowed to
450 grow in culture medium containing 10% FBS for 24 h. The cells were fixed with 70% ethanol at
451 4°C overnight, and were incubated with Propidium Iodide (PI)/RNase Staining Solution (#4087S,
452 Cell Signaling Technologies) for 30 min. After incubation, cell cycle was analyzed using a flow
453 cytometer (BD Symphony).

454

455 Cell apoptosis assay

456 Cells were harvested and then incubated with 7-AAD (#420404, BioLegend) and Annexin-V
457 (#640926, BioLegend) at room temperature for 10-20 min. After incubation, cell apoptosis was
458 analyzed using a flow cytometer (BD Symphony).
459
460 Cell migration and invasion assays in Boyden chambers
461 As described previously (Xiao et al., 2023), $1*10^5$ cells were seeded in the upper wells of
462 Transwell for migration and Matrigel-coated Boyden chambers for invasion assays, respectively
463 (BD Biosciences) and allowed to migrate toward 10% FBS in the bottom wells. After 16 h of
464 incubation, migrating or invading cells were stained with 0.1% crystal violet, photographed, and
465 counted. For conditioned medium (CM) transfer experiments, CM samples were isolated, filtered
466 through a 0.45-μm filter, and applied to cells seeded in the upper wells.
467
468 Liquid chromatography/mass spectrometry (LC-MS)
469 The immunoprecipitation (IP) from agarose beads was then washed with ice-cold lysis buffer 5
470 times. The bound proteins on beads were eluted in 5% SDS. For mass spectrometry analysis,
471 samples were reduced, alkylated, and digested using trypsin on an S-trap as described
472 (Mascibroda et al., 2022). The resultant peptides were quantified and normalized within sets by
473 the Quantitative Fluorometric Peptide Assay. Samples were analyzed using a 90-minute gradient
474 on our Orbitrap Eclipse. The resulting Liquid chromatography-mass spectrometry (LC-MS) data
475 was processed in Proteome Discoverer 2.5 and SEQUEST using a human database. The minora
476 node was used to perform Label-Free Quantitation (LFQ) using the MS peak areas for each of
477 the peptide-spectral matches. The IP-MS was performed in triplicate.
478
479 Immune cell profiling
480 Mouse flank tumors generated by subcutaneous injection of $0.5*10^6$ parental 344SQ or
481 344SQ_REEP2_KO #25 or #44 cells into the flank of wild-type mice for 5 weeks were harvested.

482 The tumor tissues and mouse spleens were processed for isolating tumor-infiltrating lymphocytes
483 by The Flow Cytometry and Immune Monitoring Core Facility (University of Kentucky, Lexington,
484 Kentucky). Single-cell suspension was stained as described previously (Xiao et al., 2023) with
485 the following antibodies: CD3-PE-594 (#100246, BioLegend), CD45-Pacific Blue (#103126,
486 BioLegend), CD4-APCCy7 (#100526, BioLegend), CD8-PE-Cy7 (#100721, BioLegend), CD278-
487 PE (#117406, BioLegend), CD25-BUV395 (#564022, BD Biosciences), PD1-BV-505 (#135220,
488 BioLegend), CD62L-FITC (#35-0621-U500, Thermo Fisher Scientific), CD44-BV-711 (#103057,
489 BioLegend), TIM3-APC (#134007, BioLegend), FoxP3-PerCP-Cy5.5 (#45-5773-82, Invitrogen),
490 GR1-BV-711 (#106443, BioLegend), CD11b-BV-650 (#101239, BioLegend), CD11c-BV-785
491 (#117335, BioLegend), F4/80-APC (#204801-U100, Tonbo), PDL1-PE-Dazzle-594 (#124323,
492 BioLegend), CD86-APC-Cy7 (#105030, BioLegend), MCHII-PE-Cy7 (#107629, BioLegend),
493 CD80-BV-605 (#104729, BioLegend), CD68-PerCP-Cy5.5 (#137009, BioLegend), iNOS-PE
494 (#125920-80, Invitrogen), Arg1-FITC (IC5868F, R&D Systems), CD31-BV-786 (#740870, BD
495 Biosciences), and the live/dead cell marker Ghost Violet-BV-510 (#10-0870-T100, VWR). For
496 intracellular staining, cells were fixed and permeabilized using the intracellular staining perm wash
497 buffer (BioLegend) according to manufacturer instructions. Data were acquired using a flow
498 cytometer (BD Symphony) and analyzed using FlowJo software (version 10.10.0; BD
499 Biosciences).
500
501 Analysis of Kaplan-Meier Survival Data
502 LUAD patient survival data were downloaded from the Kaplan-Meier plotter database (Gyorffy et
503 al., 2013). Analysis of LUAD patients was performed in REEP2 high- and low-expression cohorts.
504 The *P* value was calculated using the log-rank test (Gyorffy et al., 2013).
505
506 TNMplot analysis

507 The REEP2 mRNA expression analysis in normal lung and different stages of lung tumor tissues
508 was performed as previously described (Bartha and Gyorffy, 2021).
509
510 Statistical analysis
511 Unless mentioned otherwise, the results shown are representative of replicated experiments and
512 are the means ± standard error of the means (SEM) from triplicate samples or randomly chosen
513 cells within a field. The comparison of mRNA levels with EMT scores and the correlation analysis
514 in human lung cancers were performed as previously described (Gibbons and Creighton, 2018),
515 and the EMT score was calculated as previously described (Byers et al., 2013; Gibbons and
516 Creighton, 2018). Statistical evaluations were carried out with Prism 9 (GraphPad Software, Inc.).
517 Unpaired 2-tailed Student t-tests or ANOVA were used to compare means for two or more groups,
518 respectively, and P values < 0.05 were considered statistically significant.
519
520

521 **Data, materials, and software availability**

522 All data are available in the main text or the supporting information.

523

524 **Acknowledgement**

525 This work was supported by the National Institutes of Health (NIH) through R00 CA249048 (to
526 G.X.), R03 CA280382 (to X.T.), R01 CA181184 (to J.M.K.), R01 CA2111125 (to J.M.K.), NIH
527 Lung Cancer SPORE grant P50 CA70907 (to J.M.K.). We thank The Functional Genomics Core
528 (The University of Texas MD Anderson Cancer Center) for CRISPRi library virus preparation and
529 cell infection, and The Biospecimen Extraction Facility (The University of Texas MD Anderson
530 Cancer Center) for genomic DNA extraction from CRISPRi in vivo screen. This research was
531 supported by the Flow Cytometry and Immune Monitoring (FCIM) Shared Resource of the
532 University of Kentucky Markey Cancer Center (P30CA177558). We thank the FCIM for tumor
533 tissue processing for immune cell profiling.

534

535 **Author contributions**

536 K.F., O.O., and G.X. conceived, designed, executed, and interpreted all experiments. S.W. and
537 X.T. assisted with mutagenesis for 3'-UTR reporter assays. X.L. and J.Y. assisted with mouse
538 experiments for CRISPRi *in vivo* screen. J.M.K. supported and supervised the CRISPRi *in vivo*
539 screen. J.X. assisted with CRISPR/Cas9-mediated genome-editing cell line establishment. W.K.R.
540 directed and interpreted mass spectrometry experiments. X.T. and G.X. supervised the project
541 and contributed to the design and interpretation of all experiments.

542

543 **Competing Interest Statement:** J.M.K. has received consulting fees from Halozyme. All other
544 authors declare that they have no competing interests.

545

546

547 **References**

548 Ahn, Y.H., Gibbons, D.L., Chakravarti, D., Creighton, C.J., Rizvi, Z.H., Adams, H.P., Pertsemlidis,
549 A., Gregory, P.A., Wright, J.A., Goodall, G.J., *et al.* (2012). ZEB1 drives prometastatic actin
550 cytoskeletal remodeling by downregulating miR-34a expression. J Clin Invest *122*, 3170-3183.
551 Aiello, S., and Casiraghi, F. (2021). Lysophosphatidic Acid: Promoter of Cancer Progression and
552 of Tumor Microenvironment Development. A Promising Target for Anticancer Therapies? Cells
553 *10*.
554 Banerjee, P., Xiao, G.Y., Tan, X., Zheng, V.J., Shi, L., Rabassedas, M.N.B., Guo, H.F., Liu, X.,
555 Yu, J., Diao, L., *et al.* (2021). The EMT activator ZEB1 accelerates endosomal trafficking to
556 establish a polarity axis in lung adenocarcinoma cells. Nat Commun *12*, 6354.
557 Bartha, A., and Gyorffy, B. (2021). TNMplot.com: A Web Tool for the Comparison of Gene
558 Expression in Normal, Tumor and Metastatic Tissues. Int J Mol Sci *22*.
559 Boncompain, G., Divoux, S., Gareil, N., de Forges, H., Lescure, A., Latreche, L., Mercanti, V.,
560 Jollivet, F., Raposo, G., and Perez, F. (2012). Synchronization of secretory protein traffic in
561 populations of cells. Nat Methods *9*, 493-498.
562 Boncompain, G., and Perez, F. (2012). Synchronizing protein transport in the secretory pathway.
563 Curr Protoc Cell Biol *Chapter 15*, 15 19 11-15 19 16.
564 Byers, L.A., Diao, L., Wang, J., Saintigny, P., Girard, L., Peyton, M., Shen, L., Fan, Y., Giri, U.,
565 Tumula, P.K., *et al.* (2013). An epithelial-mesenchymal transition gene signature predicts
566 resistance to EGFR and PI3K inhibitors and identifies Axl as a therapeutic target for overcoming
567 EGFR inhibitor resistance. Clin Cancer Res *19*, 279-290.
568 Chen, P.H., Bendris, N., Hsiao, Y.J., Reis, C.R., Mettlen, M., Chen, H.Y., Yu, S.L., and Schmid,
569 S.L. (2017). Crosstalk between CLCb/Dyn1-Mediated Adaptive Clathrin-Mediated Endocytosis
570 and Epidermal Growth Factor Receptor Signaling Increases Metastasis. Dev Cell *40*, 278-288
571 e275.
572 Chen, Z., Jia, X., and Liu, M. (2024). REEP4 as Potential Biomarker Associated with Predictive
573 Prognosis and Immune Response in Kidney Clear Cell Carcinoma. J Cancer *15*, 4143-4155.
574 Corallino, S., Malabarba, M.G., Zobel, M., Di Fiore, P.P., and Scita, G. (2015). Epithelial-to-
575 Mesenchymal Plasticity Harnesses Endocytic Circuitries. Front Oncol *5*, 45.
576 Di Martino, R., Sticco, L., and Luini, A. (2019). Regulation of cargo export and sorting at the trans-
577 Golgi network. FEBS Lett *593*, 2306-2318.
578 Elkin, S.R., Lakoduk, A.M., and Schmid, S.L. (2016). Endocytic pathways and endosomal
579 trafficking: a primer. Wien Med Wochenschr *166*, 196-204.
580 Esteves, T., Durr, A., Mundwiller, E., Loureiro, J.L., Boutry, M., Gonzalez, M.A., Gauthier, J., El-
581 Hachimi, K.H., Depienne, C., Muriel, M.P., *et al.* (2014). Loss of association of REEP2 with
582 membranes leads to hereditary spastic paraplegia. Am J Hum Genet *94*, 268-277.
583 Evergren, E., Mills, I.G., and Kennedy, G. (2024). Adaptations of membrane trafficking in cancer
584 and tumorigenesis. J Cell Sci *137*.
585 Fan, S., Liu, H., and Li, L. (2022). The REEP family of proteins: Molecular targets and role in
586 pathophysiology. Pharmacol Res *185*, 106477.
587 Ferreira, A., Castanheira, P., Escrevente, C., Barral, D.C., and Barona, T. (2024). Membrane
588 trafficking alterations in breast cancer progression. Front Cell Dev Biol *12*, 1350097.
589 Gibbons, D.L., and Creighton, C.J. (2018). Pan-cancer survey of epithelial-mesenchymal
590 transition markers across the Cancer Genome Atlas. Dev Dyn *247*, 555-564.
591 Gibbons, D.L., Lin, W., Creighton, C.J., Rizvi, Z.H., Gregory, P.A., Goodall, G.J., Thilaganathan,
592 N., Du, L., Zhang, Y., Pertsemlidis, A., *et al.* (2009). Contextual extracellular cues promote tumor
593 cell EMT and metastasis by regulating miR-200 family expression. Genes Dev *23*, 2140-2151.
594 Gyorffy, B., Surowiak, P., Budczies, J., and Lanczky, A. (2013). Online survival analysis software
595 to assess the prognostic value of biomarkers using transcriptomic data in non-small-cell lung
596 cancer. PLoS One *8*, e82241.

597 Horlbeck, M.A., Gilbert, L.A., Villalta, J.E., Adamson, B., Pak, R.A., Chen, Y., Fields, A.P., Park,
598 C.Y., Corn, J.E., Kampmann, M.*, et al.* (2016). Compact and highly active next-generation
599 libraries for CRISPR-mediated gene repression and activation. Elife *5*.
600 Huang, D., Pei, Y., Dai, C., Huang, Y., Chen, H., Chen, X., Zhang, X., Lin, C., Wang, H., Zhang,
601 R.*, et al.* (2019). Up-regulated ADP-Ribosylation factor 3 promotes breast cancer cell proliferation
602 through the participation of FOXO1. Exp Cell Res *384*, 111624.
603 Hughes, H., Budnik, A., Schmidt, K., Palmer, K.J., Mantell, J., Noakes, C., Johnson, A., Carter,
604 D.A., Verkade, P., Watson, P.*, et al.* (2009). Organisation of human ER-exit sites: requirements
605 for the localisation of Sec16 to transitional ER. J Cell Sci *122*, 2924-2934.
606 Hurt, C.M., Bjork, S., Ho, V.K., Gilsbach, R., Hein, L., and Angelotti, T. (2014). REEP1 and REEP2
607 proteins are preferentially expressed in neuronal and neuronal-like exocytotic tissues. Brain Res
608 *1545*, 12-22.
609 Kato, K., Yoshikawa, K., Tanabe, E., Kitayoshi, M., Fukui, R., Fukushima, N., and Tsujiuchi, T.
610 (2012). Opposite roles of LPA1 and LPA3 on cell motile and invasive activities of pancreatic
611 cancer cells. Tumour Biol *33*, 1739-1744.
612 Lakoduk, A.M., Roudot, P., Mettlen, M., Grossman, H.M., Schmid, S.L., and Chen, P.H. (2019).
613 Mutant p53 amplifies a dynamin-1/APPL1 endosome feedback loop that regulates recycling and
614 migration. J Cell Biol *218*, 1928-1942.
615 Lanzetti, L., and Di Fiore, P.P. (2008). Endocytosis and cancer: an 'insider' network with
616 dangerous liaisons. Traffic *9*, 2011-2021.
617 Li, B., Severson, E., Pignon, J.C., Zhao, H., Li, T., Novak, J., Jiang, P., Shen, H., Aster, J.C.,
618 Rodig, S.*, et al.* (2016). Comprehensive analyses of tumor immunity: implications for cancer
619 immunotherapy. Genome Biol *17*, 174.
620 Li, T., Fan, J., Wang, B., Traugh, N., Chen, Q., Liu, J.S., Li, B., and Liu, X.S. (2017). TIMER: A
621 Web Server for Comprehensive Analysis of Tumor-Infiltrating Immune Cells. Cancer Res *77*,
622 e108-e110.
623 Li, T., Fu, J., Zeng, Z., Cohen, D., Li, J., Chen, Q., Li, B., and Liu, X.S. (2020). TIMER2.0 for
624 analysis of tumor-infiltrating immune cells. Nucleic Acids Res *48*, W509-W514.
625 Liberali, P., Snijder, B., and Pelkmans, L. (2014). A hierarchical map of regulatory genetic
626 interactions in membrane trafficking. Cell *157*, 1473-1487.
627 Linstedt, A.D., Jesch, S.A., Mehta, A., Lee, T.H., Garcia-Mata, R., Nelson, D.S., and Sztul, E.
628 (2000). Binding relationships of membrane tethering components. The giantin N terminus and the
629 GM130 N terminus compete for binding to the p115 C terminus. J Biol Chem *275*, 10196-10201.
630 Liu, S., Murph, M., Panupinthu, N., and Mills, G.B. (2009). ATX-LPA receptor axis in inflammation
631 and cancer. Cell Cycle *8*, 3695-3701.
632 Makaraci, P., and Kim, K. (2018). trans-Golgi network-bound cargo traffic. Eur J Cell Biol *97*, 137-
633 149.
634 Martin, T.D., Patel, R.S., Cook, D.R., Choi, M.Y., Patil, A., Liang, A.C., Li, M.Z., Haigis, K.M., and
635 Elledge, S.J. (2021). The adaptive immune system is a major driver of selection for tumor
636 suppressor gene inactivation. Science *373*, 1327-1335.
637 Mascibroda, L.G., Shboul, M., Elrod, N.D., Colleaux, L., Hamamy, H., Huang, K.L., Peart, N.,
638 Singh, M.K., Lee, H., Merriman, B.*, et al.* (2022). INTS13 variants causing a recessive
639 developmental ciliopathy disrupt assembly of the Integrator complex. Nat Commun *13*, 6054.
640 Maxfield, F.R., and McGraw, T.E. (2004). Endocytic recycling. Nat Rev Mol Cell Biol *5*, 121-132.
641 Mosesson, Y., Mills, G.B., and Yarden, Y. (2008). Derailed endocytosis: an emerging feature of
642 cancer. Nat Rev Cancer *8*, 835-850.
643 Park, C.R., You, D.J., Park, S., Mander, S., Jang, D.E., Yeom, S.C., Oh, S.H., Ahn, C., Lee, S.H.,
644 Seong, J.Y.*, et al.* (2016). The accessory proteins REEP5 and REEP6 refine CXCR1-mediated
645 cellular responses and lung cancer progression. Sci Rep *6*, 39041.

Pelkmans, L., Fava, E., Grabner, H., Hannus, M., Habermann, B., Krausz, E., and Zerial, M. (2005). Genome-wide analysis of human kinases in clathrin- and caveolae/raft-mediated endocytosis. Nature *436*, 78-86.

Pietrobono, S., Sabbadini, F., Bertolini, M., Mangiameli, D., De Vita, V., Fazzini, F., Lunardi, G., Casalino, S., Scarlato, E., Merz, V.*, et al.* (2024). Autotaxin Secretion Is a Stromal Mechanism of Adaptive Resistance to TGFbeta Inhibition in Pancreatic Ductal Adenocarcinoma. Cancer Res *84*, 118-132.

Reis, C.R., Chen, P.H., Srinivasan, S., Aguet, F., Mettlen, M., and Schmid, S.L. (2015). Crosstalk between Akt/GSK3beta signaling and dynamin-1 regulates clathrin-mediated endocytosis. EMBO J *34*, 2132-2146.

Robinson, C.M., Duggan, A., and Forrester, A. (2024). ER exit in physiology and disease. Front Mol Biosci *11*, 1352970.

Schmid, S.L. (2017). Reciprocal regulation of signaling and endocytosis: Implications for the evolving cancer cell. J Cell Biol *216*, 2623-2632.

Shibata, Y., Mazur, E.E., Pan, B., Paulo, J.A., Gygi, S.P., Chavan, S., Valerio, L.S.A., Zhang, J., and Rapoport, T.A. (2024). The membrane curvature-inducing REEP1-4 proteins generate an ER-derived vesicular compartment. Nat Commun *15*, 8655.

Sprangers, J., and Rabouille, C. (2015). SEC16 in COPII coat dynamics at ER exit sites. Biochem Soc Trans *43*, 97-103.

Szul, T., and Sztul, E. (2011). COPII and COPI traffic at the ER-Golgi interface. Physiology (Bethesda) *26*, 348-364.

Tan, X., Banerjee, P., Guo, H.F., Ireland, S., Pankova, D., Ahn, Y.H., Nikolaidis, I.M., Liu, X., Zhao, Y., Xue, Y.*, et al.* (2017). Epithelial-to-mesenchymal transition drives a pro-metastatic Golgi compaction process through scaffolding protein PAQR11. J Clin Invest *127*, 117-131.

Tan, X., Banerjee, P., Liu, X., Yu, J., Gibbons, D.L., Wu, P., Scott, K.L., Diao, L., Zheng, X., Wang, J.*, et al.* (2018). The epithelial-to-mesenchymal transition activator ZEB1 initiates a prometastatic competing endogenous RNA network. J Clin Invest *128*, 1267-1282.

Tan, X., Banerjee, P., Shi, L., Xiao, G.Y., Rodriguez, B.L., Grzeskowiak, C.L., Liu, X., Yu, J., Gibbons, D.L., Russell, W.K.*, et al.* (2021). p53 loss activates prometastatic secretory vesicle biogenesis in the Golgi. Sci Adv *7*.

Tan, X., Xiao, G.Y., Banerjee, P., Wang, S., and Kurie, J.M. (2024). The cancer-associated secretory phenotype: a new frontier in targeted therapeutics. J Clin Invest *134*.

Tan, X., Xiao, G.Y., Wang, S., Shi, L., Zhao, Y., Liu, X., Yu, J., Russell, W.K., Creighton, C.J., and Kurie, J.M. (2023). EMT-activated secretory and endocytic vesicular trafficking programs underlie a vulnerability to PI4K2A antagonism in lung cancer. J Clin Invest *133*.

Tejeda-Munoz, N., Mei, K.C., Sheladiya, P., and Monka, J. (2022). Targeting Membrane Trafficking as a Strategy for Cancer Treatment. Vaccines (Basel) *10*.

Tseng, C.C., Hung, C.C., Shu, C.W., Lee, C.H., Chen, C.F., Kuo, M.S., Kao, Y.Y., Chen, C.L., Ger, L.P., and Liu, P.F. (2023). The Clinical and Biological Effects of Receptor Expression-Enhancing Protein 6 in Tongue Squamous Cell Carcinoma. Biomedicines *11*.

Waguri, S., Dewitte, F., Le Borgne, R., Rouille, Y., Uchiyama, Y., Dubremetz, J.F., and Hoflack, B. (2003). Visualization of TGN to endosome trafficking through fluorescently labeled MPR and AP-1 in living cells. Mol Biol Cell *14*, 142-155.

Weber, R., Groth, C., Lasser, S., Arkhypov, I., Petrova, V., Altevogt, P., Utikal, J., and Umansky, V. (2021). IL-6 as a major regulator of MDSC activity and possible target for cancer immunotherapy. Cell Immunol *359*, 104254.

Weigel, A.V., Chang, C.L., Shtengel, G., Xu, C.S., Hoffman, D.P., Freeman, M., Iyer, N., Aaron, J., Khuon, S., Bogovic, J.*, et al.* (2021). ER-to-Golgi protein delivery through an interwoven, tubular network extending from ER. Cell *184*, 2412-2429 e2416.

695 Xiao, G.Y., Mohanakrishnan, A., and Schmid, S.L. (2018). Role for ERK1/2-dependent activation
696 of FCHSD2 in cancer cell-selective regulation of clathrin-mediated endocytosis. Proc Natl Acad
697 Sci U S A *115*, E9570-E9579.
698 Xiao, G.Y., and Schmid, S.L. (2020). FCHSD2 controls oncogenic ERK1/2 signaling outcome by
699 regulating endocytic trafficking. PLoS Biol *18*, e3000778.
700 Xiao, G.Y., Tan, X., Rodriguez, B.L., Gibbons, D.L., Wang, S., Wu, C., Liu, X., Yu, J., Vasquez,
701 M.E., Tran, H.T., *et al.* (2023). EMT activates exocytotic Rabs to coordinate invasion and
702 immunosuppression in lung cancer. Proc Natl Acad Sci U S A *120*, e2220276120.
703 Yu, S., Murph, M.M., Lu, Y., Liu, S., Hall, H.S., Liu, J., Stephens, C., Fang, X., and Mills, G.B.
704 (2008). Lysophosphatidic acid receptors determine tumorigenicity and aggressiveness of ovarian
705 cancer cells. J Natl Cancer Inst *100*, 1630-1642.
706 Zuchner, S., Wang, G., Tran-Viet, K.N., Nance, M.A., Gaskell, P.C., Vance, J.M., Ashley-Koch,
707 A.E., and Pericak-Vance, M.A. (2006). Mutations in the novel mitochondrial protein REEP1 cause
708 hereditary spastic paraplegia type 31. Am J Hum Genet *79*, 365-369.
709

710

Figures

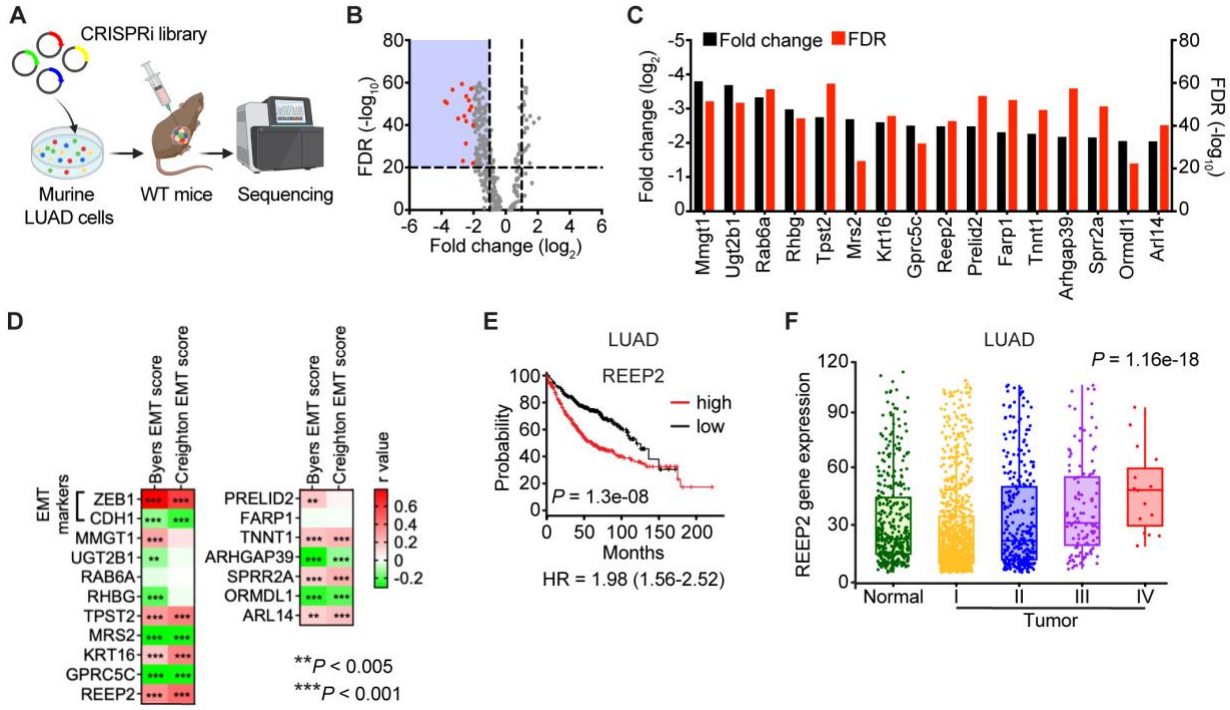

Figure 1. Pro-tumorigenic membrane trafficking program for LUAD growth. (A) A CRISPRi library targeting membrane trafficking genes was transduced into 344SQ murine LUAD cells. Cells were transplanted subcutaneously on the flanks of WT syngeneic mice. Following tumor formation, the tumors were harvested and sgRNAs were sequenced. (B) Volcano plots of the analyses of the screening results in immunocompetent WT mice. Grey dots represent membrane trafficking genes, and vertical and horizontal dotted lines indicate fold-change ($\log_2$) = ±1 and FDR ($-\log_{10}$) = 20, respectively. The red dots represent the top hits that fold-change ($\log_2$) < -2 and FDR ($-\log_{10}$) > 20. (C) The bar graph represents the top hits in (B) (Red dots). (D) Heat map illustration of correlation between mRNA levels of indicated genes and EMT scores (Byers or Creighton) in the TCGA LUAD cohort. r values: Pearson correlation. (E) Kaplan-Meier survival analysis of LUAD patients based on REEP2 mRNA levels above (high) or below (low) the median value. (F) Expression levels of REEP2 mRNA in normal lung tissues (n = 391), stage I (n = 905), stage II (n = 331), stage III (n = 146), and stage IV lung tumors (n = 17) using data from TNMplot. (https://tnmplot.com/).

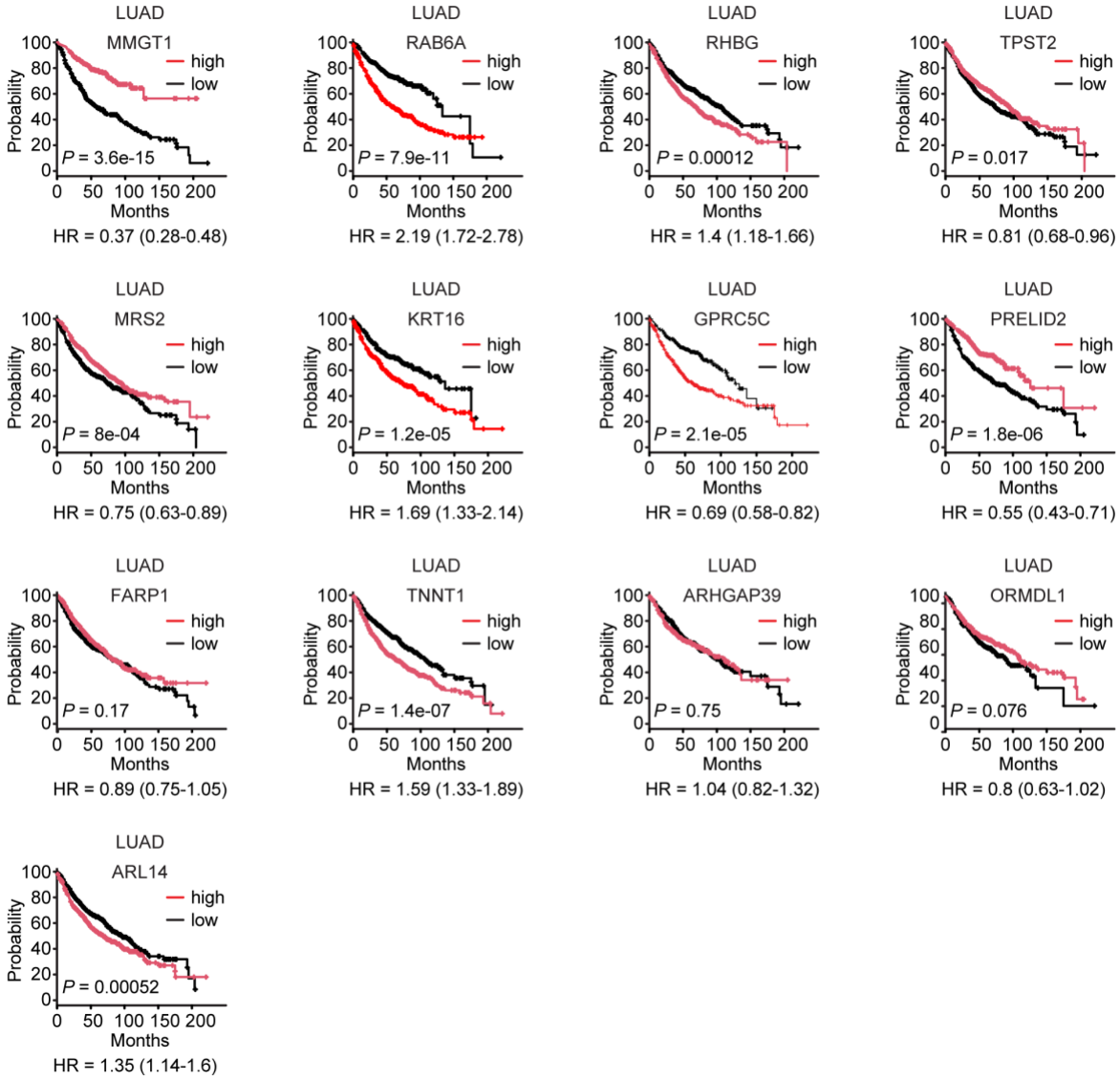

Fig. S1. Kaplan-Meier survival analysis of LUAD patients based on the mRNA levels of indicated genes above (high) or below (low) the median value.

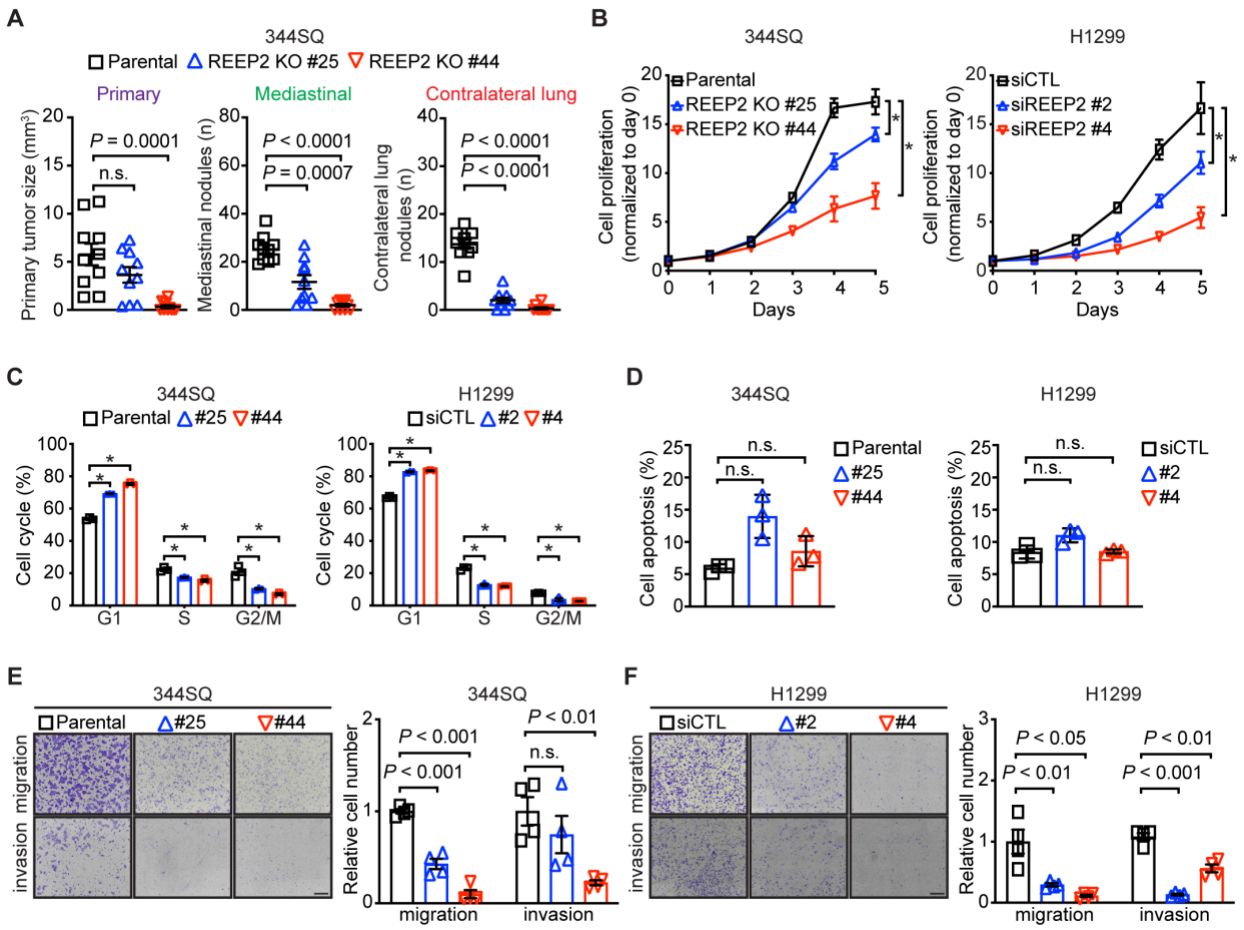

Figure 2. REEP2 is critical for EMT-driven LUAD progression. (A) Syngeneic, immunocompetent mice were injected with parental or REEP2 KO 344SQ cells and necropsies were performed 2 weeks later to assess tumor formation and metastasis (n = 10 mice per cohort). Orthotopic lung tumor size (left dot plot) and numbers of metastases to mediastinum (middle dot plot) and contralateral lung (right dot plot). (B) *In vitro* cell proliferation assay in murine 344SQ parental and REEP2 knockout (KO) cells, and human H1299 cells transfected with control siRNA (siCTL) or REEP2 siRNA (siREEP2). (C, D) Analyses of cell cycle (C) and apoptosis (D) in murine 344SQ parental and REEP2 knockout (KO) cells, and human H1299 cells with siRNA-mediated REEP2 knockdown (siREEP2). (E, F) Bright-field micrographs of crystal violet-stained murine (344SQ) (E) and human (H1299) (F) cells that migrated through noncoated (migration) or Matrigel-coated (invasion) filters in Boyden chambers. The scatter plots represent the

787 quantification of replicates 16 h after seeding and normalized to parental. Results represent

788 means ± SEM. *P* values were determined using two-tailed Student's t-test.

789

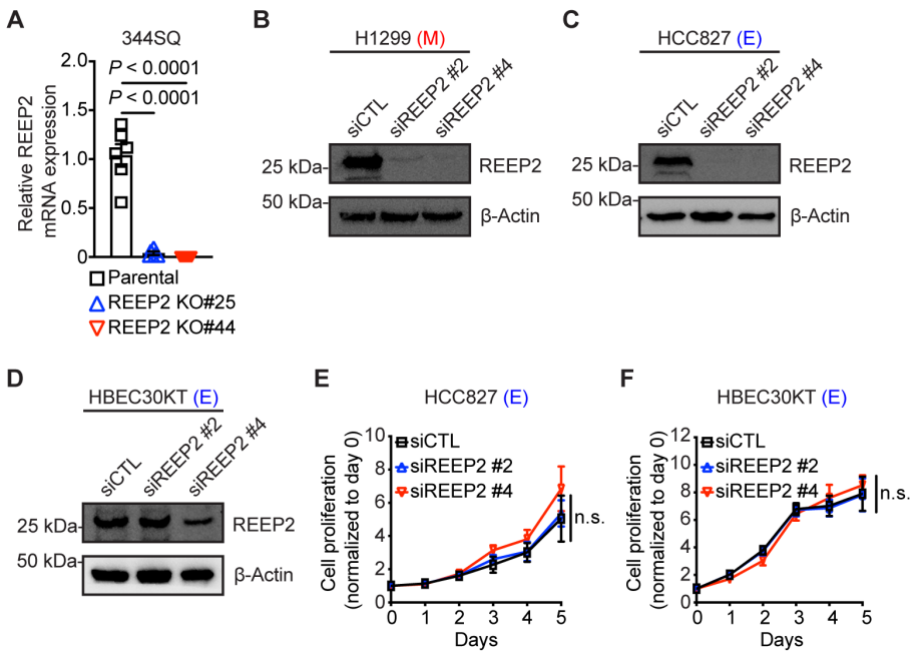

Figure S2. Depletion of REEP2 in murine and human LUAD cells. (A) qPCR analysis of REEP2 mRNA expression levels in parental or REEP2 knockout (KO) 344SQ cell lines (n=6 replicates per condition). (B-D) WB analysis of REEP2 levels in human H1299 (B), HCC827 (C), and HBEC30KT (D) cells transfected with control siRNA (siCTL) or REEP2 siRNA (siREEP2). β-Actin loading control. M: mesenchymal. E: epithelial. (E, F) *In vitro* cell proliferation assay in human HCC827 (E) and HBEC30KT (F) cells transfected with control siRNA (siCTL) or REEP2 siRNA (siREEP2). Results represent means ± SEM. *P* values were determined using two-tailed Student's t-test.

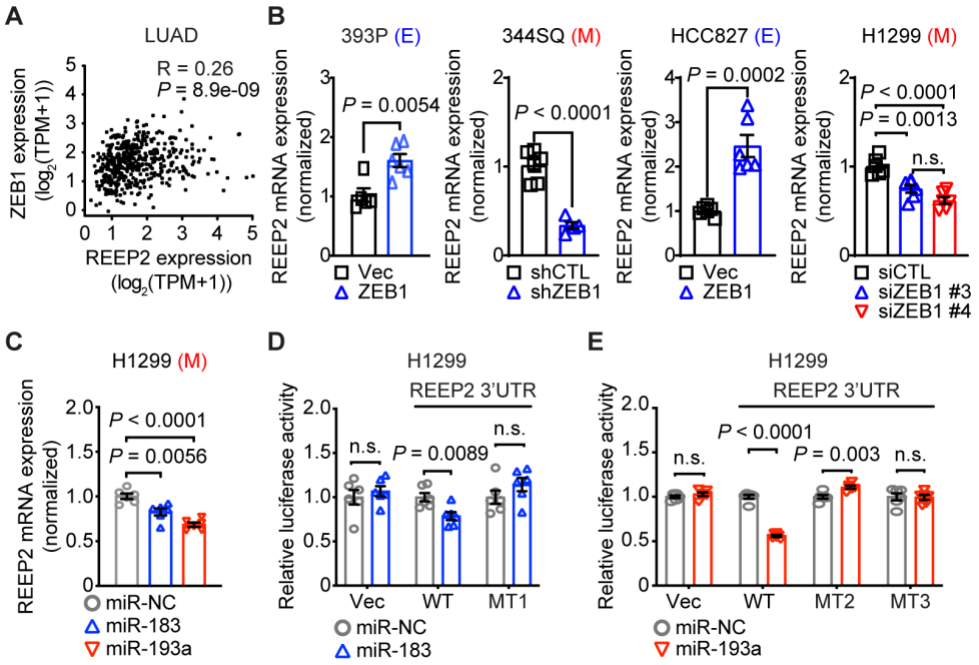

Figure 3. ZEB1 activates REEP2 via miRNAs. (A) The correlation between REEP2 and ZEB1 mRNA expression (TPM (transcripts per million)) in TCGA LUAD tissues. R, Spearman correlation. (B) qPCR analysis of REEP2 mRNA expression levels in murine (393P, 344SQ) and human (HCC827, H1299) LUAD cells with ectopic ZEB1-expression or ZEB1-depletion (n=6 replicates per condition). Vec: empty vector. E: epithelial. M: mesenchymal. (C) qPCR analysis of REEP2 mRNA expression levels in miR mimic-transfected human LUAD cells. NC: non-coding control. M: mesenchymal. (D, E) Human REEP2 3'-UTR reporter assays. Luciferase activities in H1299 cells transiently co-transfected with pre-miRs of miR-183 (D) or miR-193a (E) and human REEP2 3'UTR reporters containing wild-type (WT) or mutant 3'-UTRs lacking predicted miR-binding sites (MT1-3). Vec: empty vector. Results represent means ± SEM. *P* values were determined using two-tailed Student's t-test.

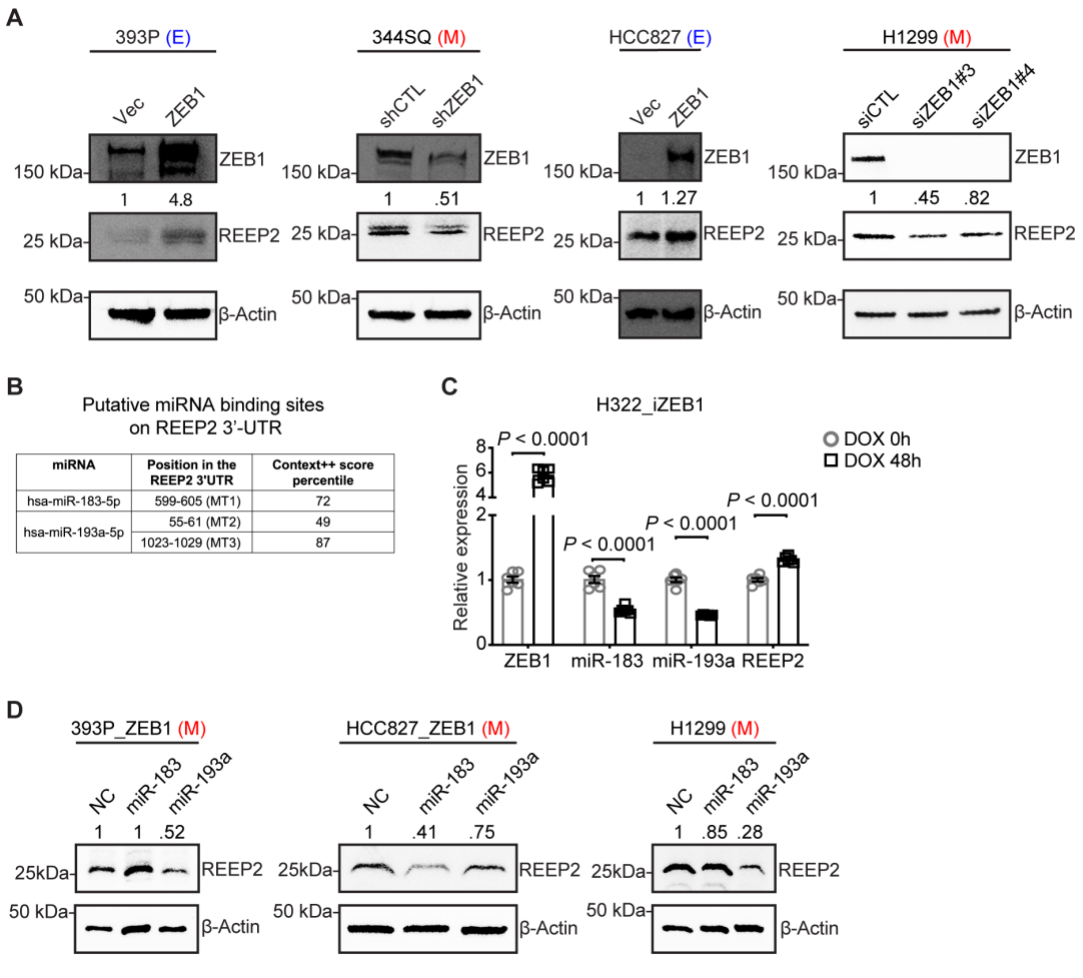

Figure S3. ZEB1 upregulates REEP2 through the regulation of miRNAs. (A) WB analysis of ZEB1 and REEP2 protein expression levels in murine (393P, 344SQ) and human (HCC827, H1299) LUAD cells with ectopic ZEB1-expression or ZEB1-depletion. β-actin loading control. Relative densitometric values are indicated. E: epithelial. M: mesenchymal. (B) Putative miRNA binding sites on REEP2 3'UTR predicted by TargetScan and used for mutagenesis (MT1-3) (C) qPCR analysis of ZEB1, miR-183, miR-193a, and REEP2 expression levels in human H322_iZEB1 cells with doxycycline (DOX) (1 μg/ml) treatment (n=6 replicates per condition). Results represent means ± SEM. *P* values were determined using two-tailed Student's t-test. (D) WB analysis of REEP2 protein expression levels in the indicated cells transfected with miR-183 or miR-193a mimics or non-coding control (NC). M: mesenchymal.

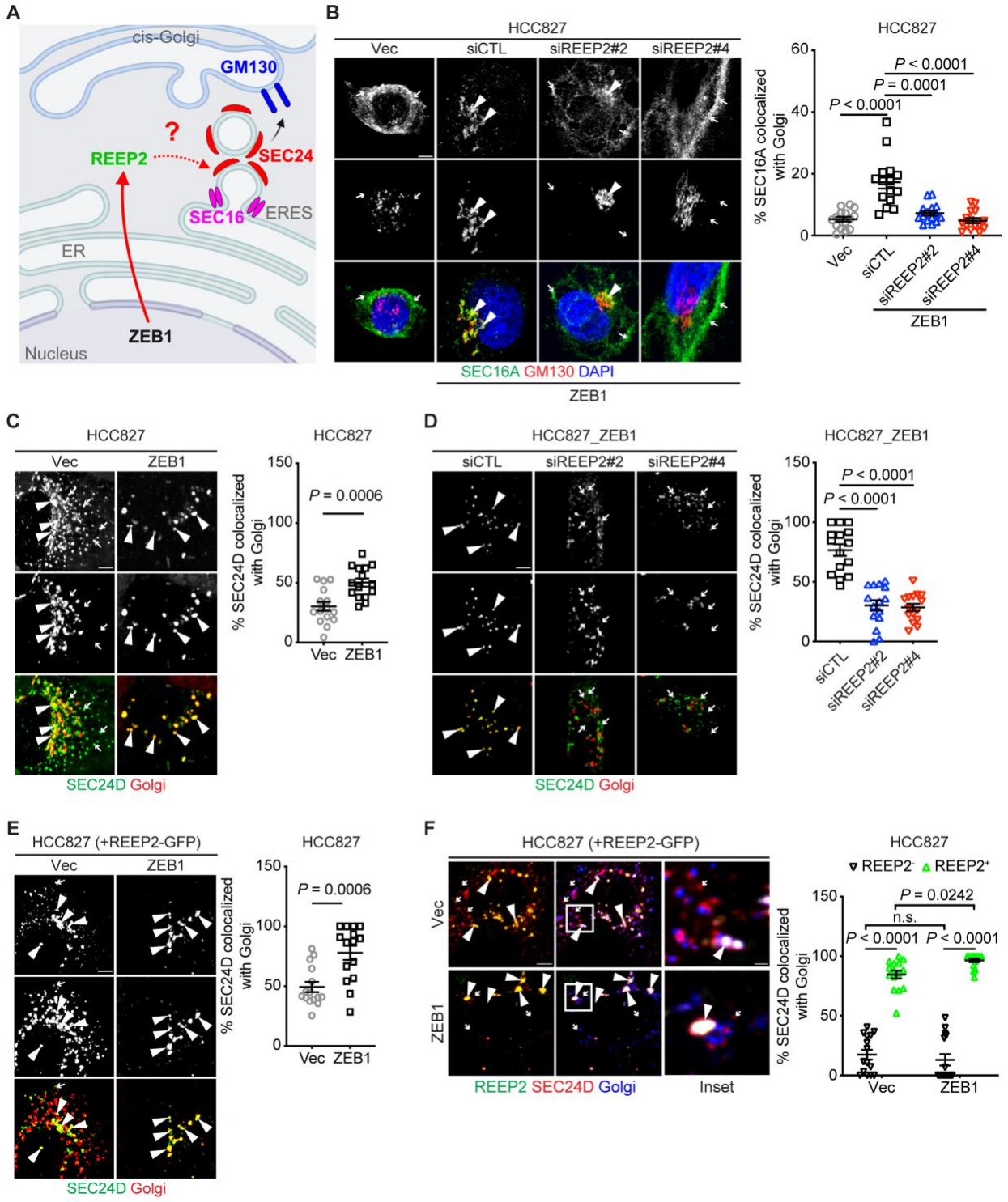

Figure 4. ZEB1 coordinates REEP2 to promote ERES colocalization with the Golgi. (A) Schematic illustration of a secretory pathway model. ZEB1 upregulates REEP2 to promote ERES (SEC16, SEC24) transportation to the Golgi (GM130). (B) Confocal micrographs of cells co-

886 stained with anti-SEC16A (green) and anti-GM130 (red) antibodies. DAPI (blue). Scale bar: 5 μm.
887 The scatter plots quantify Golgi-localized SEC16A per cell (dot) based on % of total SEC16A that
888 co-localizes with Golgi (GM130 channel) (n = 15 cells per group). (C-E) Confocal micrographs of
889 cells co-transfected with SEC24D-mCherry (green) and Golgi- pmTurquoise2 (red). DAPI (blue).
890 Scale bar: 5 μm. The scatter plots quantify Golgi-localized SEC24D per cell (dot) based on % of
891 total SEC24D that co-localizes with Golgi (n = 15 cells per group) in HCC827 cells with ectopic
892 ZEB1-expression (C), and with REEP2 depletion (D) or REEP2-GFP transfection (E). (F)
893 Confocal micrographs of cells co-transfected with REEP2-GFP (green), SEC24D-mCherry (red)
894 and Golgi- pmTurquoise2 (blue). Scale bar: 5 μm, 1 μm (inset). The scatter plots quantify Golgi-
895 localized SEC24D per cell (dot) based on % of total SEC24D that co-localizes with Golgi (n = 15
896 cells per group) in HCC827 cells with REEP2-GFP transfection. Results represent means ± SEM.
897 *P* values were determined using two-tailed Student's t-test.
898
899

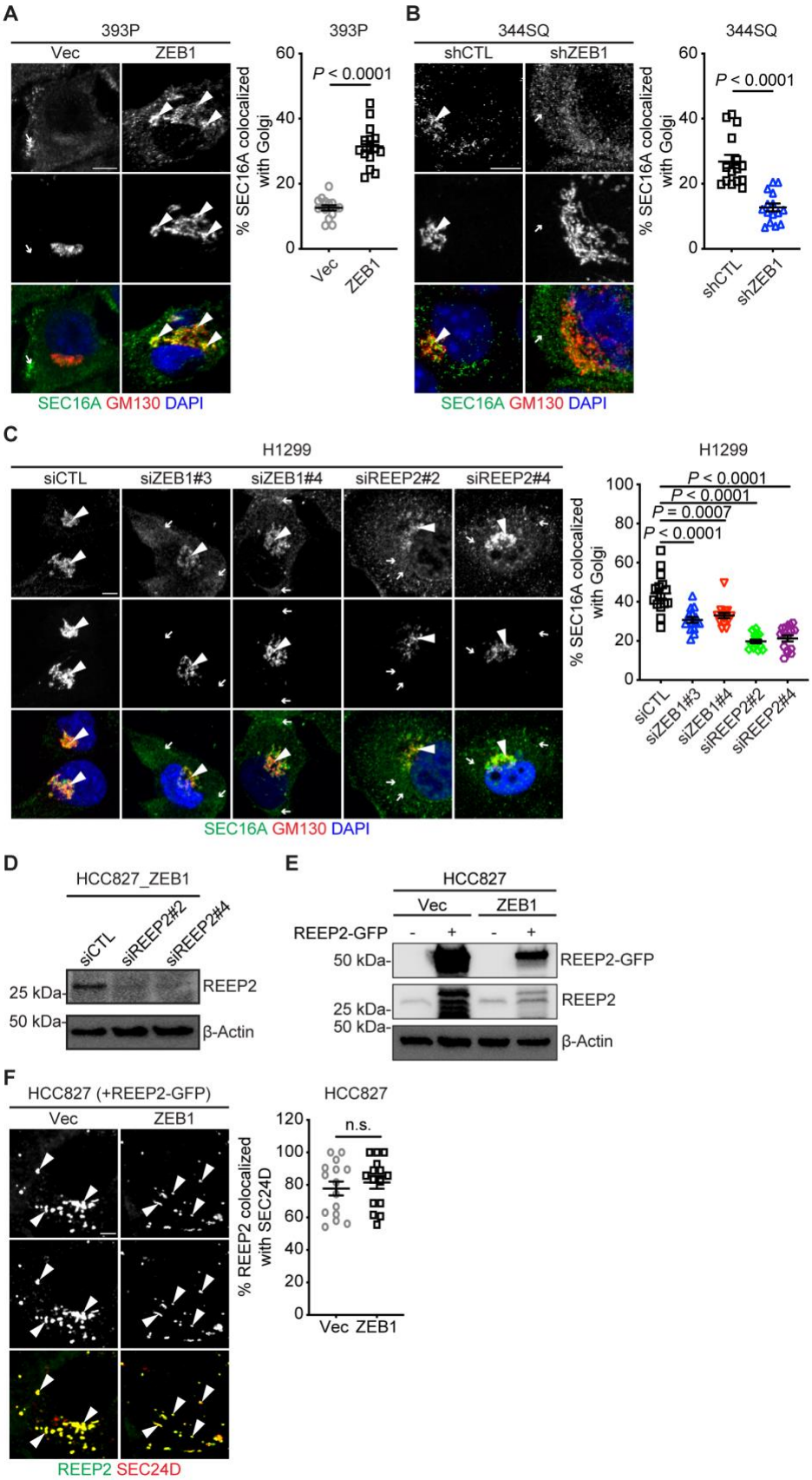
A
393P
Vec
ZEB1
393P
P < 0.0001
% SEC16A colocalized with Golgi
Vec
ZEB1
SEC16A GM130 DAPI
B
344SQ
shCTL
shZEB1
344SQ
P < 0.0001
% SEC16A colocalized with Golgi
shCTL
shZEB1
SEC16A GM130 DAPI
C
H1299
siCTL
siZEB1#3
siZEB1#4
siREEP2#2
siREEP2#4
H1299
P < 0.0001
P < 0.0001
P = 0.0007
P < 0.0001
% SEC16A colocalized with Golgi
siCTL
siZEB1#3
siZEB1#4
siREEP2#2
siREEP2#4
SEC16A GM130 DAPI
D
HCC827_ZEB1
siCTL
siREEP2#2
siREEP2#4
25 kDa-
REEP2
50 kDa-
β-Actin
E
HCC827
Vec
ZEB1
REEP2-GFP
- + - +
50 kDa-
REEP2-GFP
25 kDa-
REEP2
50 kDa-
β-Actin
F
HCC827 (+REEP2-GFP)
Vec
ZEB1
HCC827
n.s.
% REEP2 colocalized with SEC24D
Vec ZEB1
REEP2 SEC24D

925 **Figure S4. ZEB1 drives ERES colocalization with the Golgi via REEP2.** (A-C) Confocal
926 micrographs of cells co-stained with anti-SEC16A (green) and anti-GM130 (red) antibodies. DAPI
927 (blue). Scale bar: 5 μm. The scatter plots quantify Golgi-localized SEC16A per cell (dot) based
928 on % of total SEC16A that co-localizes with Golgi (GM130 channel) (n = 15 cells per group) in
929 murine epithelial cells (393P) with ectopic ZEB1-expression (A), in murine mesenchymal cells
930 (344SQ) with ZEB1 depletion (B), or in human mesenchymal cells (H1299) with ZEB1 or REEP2
931 depletions (C). (D) WB analysis of REEP2 protein expression levels in HCC827_ZEB1 cells
932 transfected with control siRNA (siCTL) or REEP2 siRNA (siREEP2). β-actin loading control. (E)
933 WB analysis of REEP2 protein expression levels in HCC827 cells co-transfected with empty
934 vector (Vec) or ZEB1, with REEP2-GFP. β-actin loading control. (F) Confocal micrographs of cells
935 co-transfected with REEP2-GFP (green) and SEC24D-mCherry (red). Scale bar: 5 μm. The
936 scatter plots quantify SEC24D-localized REEP2 per cell (dot) based on % of total REEP2 that co-
937 localizes with SEC24D (n = 15 cells per group) in HCC827 cells with ectopic ZEB1-expression.
938 Results represent means ± SEM. *P* values were determined using two-tailed Student's t-test.
939
940

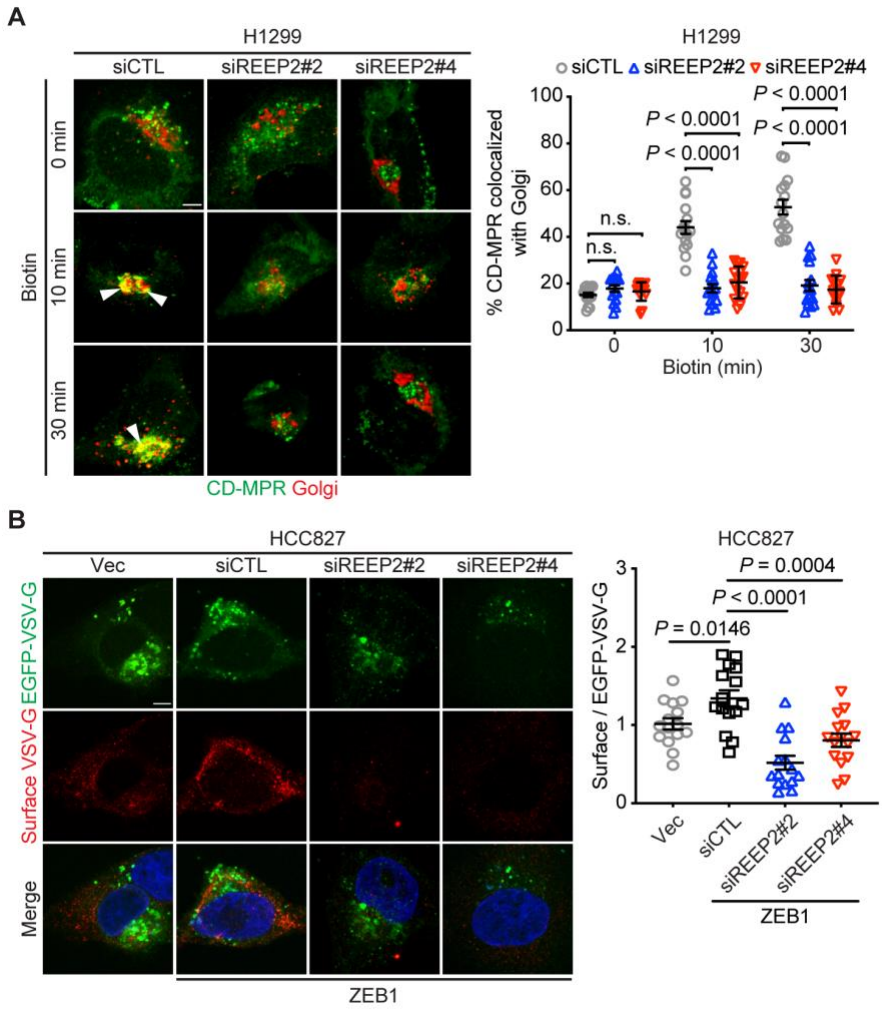

Figure 5. REEP2 promotes ER-to-Golgi trafficking. (A) Confocal micrographs of cells co-transfected with CD-MPR-RUSH-GFP (green) and Golgi-pmTurquoise2 (red). Scale bar: 5 μm. The scatter plots quantify Golgi-localized CD-MPR per cell (dot) based on % of total CD-MPR that co-localizes with Golgi at different time points after biotin treatment (40 μM) (n = 15 cells per group) in H1299 cells transfected with control siRNA (siCTL) or REEP2 siRNA (siREEP2). (B) Confocal micrographs of EGFP-VSV-G-transfected cells taken 1 h after transfer to permissive temperature. Scale bar, 5 μm. The scatter plot represents the ratio of surface VSV-G to EGFP-VSV-G in each cell (dot) (n = 15 cells per group) in HCC827 cells co-transfected with empty vector (Vec) or ZEB1 with control siRNA (siCTL) or REEP2 siRNA (siREEP2). Results represent means ± SEM. *P* values were determined using two-tailed Student's t-test.

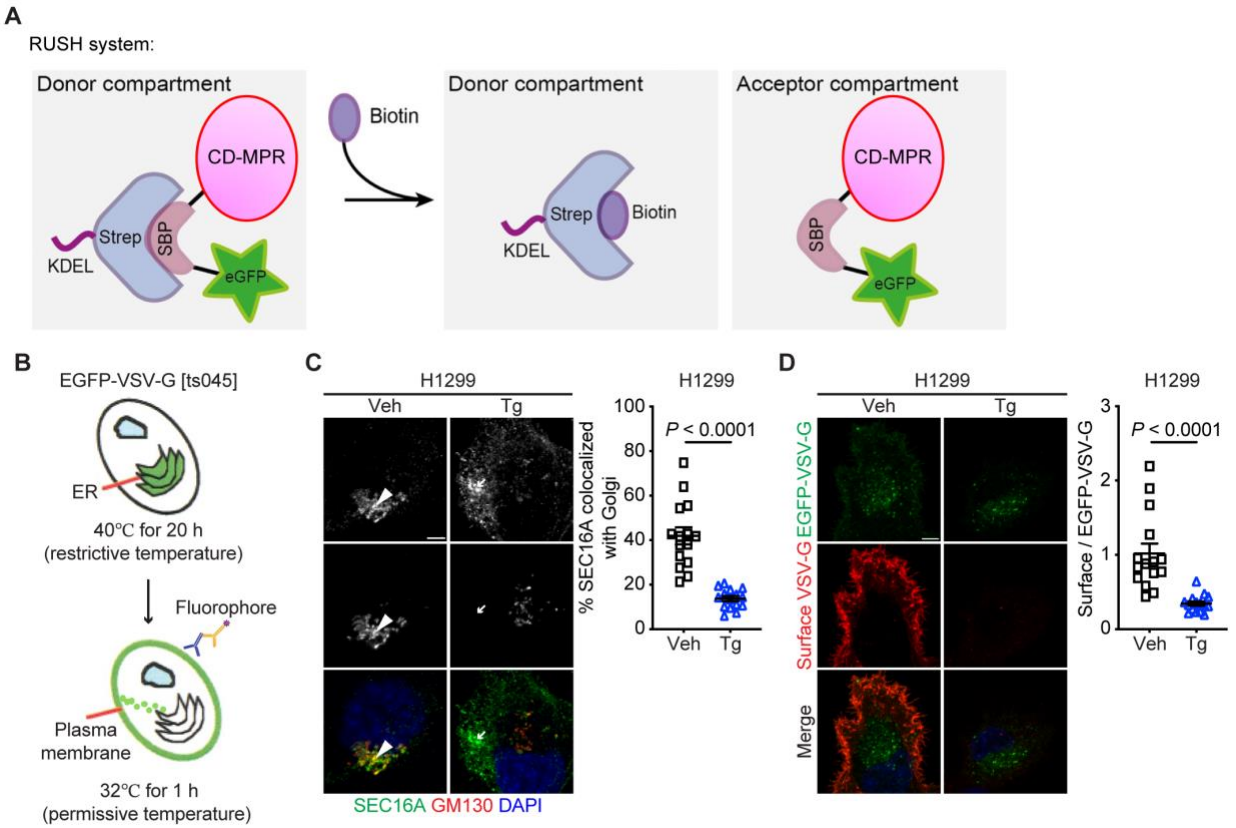

Figure S5. ERES/Golgi colocalization promotes secretory trafficking. (A) Schematic illustration of the retention using selective hooks (RUSH) system. The cells were co-transfected with the reporter protein (CD-MPR), which is fused to the streptavidin-binding peptide (SBP) and GFP, and a second protein with a C-terminal ER retention signal (Lys-Asp-Glu-Leu; KDEL) fusing with streptavidin as a hook. The interaction of CD-MPR with the hook protein retains CD-MPR in the ER compartment and biotin administration releases the CD-MPR-GFP reporter from the ER and transfers it to the Golgi. (B) Schematic of VSV-G assay. The cells were transfected with vectors that express an EGFP-tagged temperature-sensitive mutant VSV-G (EGFP-VSV-G [ts045]) that is transported from the ER to the plasma membrane via the Golgi. At designated time points after switching cells to temperatures that cause VSV-G accumulation (40°C) and release (32°C) from the ER, cells were fixed and exofacial VSV-G was detected in non-permeabilized cells by staining with anti-VSV-G monoclonal antibody. The VSV-G trafficking to the plasma membrane is determined by the ratio of exofacial (surface) VSV-G fluorescence signal to the

966 EGFP signal intensity. (C) Confocal micrographs of cells co-stained with anti-SEC16A (green)
967 and anti-GM130 (red) antibodies. DAPI (blue). Scale bar: 5 μm. The scatter plots quantify Golgi-
968 localized SEC16A per cell (dot) based on % of total SEC16A that co-localizes with Golgi (GM130
969 channel) (n = 15 cells per group) in H1299 cells treated with vehicle control (Veh) or 5 μM
970 thapsigargin (Tg) for 1 h. (D) Confocal micrographs of EGFP-VSV-G-transfected cells taken 1 h
971 after transfer to permissive temperature. Scale bar, 5 μm. The scatter plot represents the ratio of
972 surface VSV-G to EGFP-VSV-G in each cell (dot) (n = 15 cells per group) in H1299 cells treated
973 with vehicle control (Veh) or 5 μM thapsigargin (Tg) for 1 h. Results represent means ± SEM. *P*
974 values were determined using two-tailed Student's t-test.
975
976

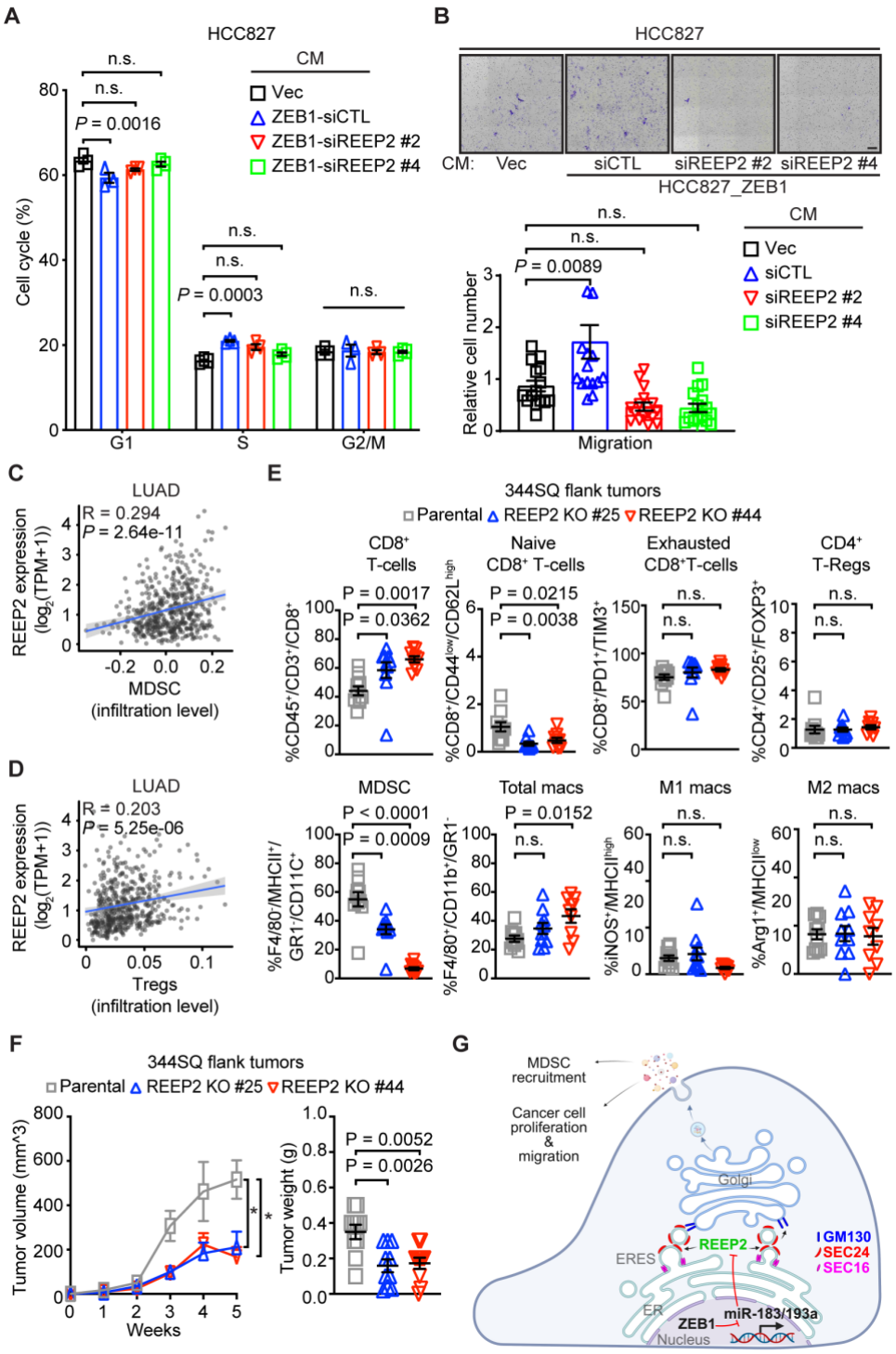

Figure 6. REEP2-driven secretome promotes LUAD progression. (A) Analyses of cell cycle in HCC827 cells treated with CM from indicated cells. (B) Bright-field micrographs of crystal violet-stained HCC827 cells that migrated through noncoated filters in Boyden chambers. Upper chambers loaded with indicated CM samples. The scatter plots represent the quantification of

1003 replicates 16 h after seeding and normalized to Vec. (C, D) Correlation of REEP2 mRNA levels
1004 with infiltration levels of myeloid-derived suppressor cells (MDSCs) (C) and regulatory T (Tregs)
1005 cells (D) quantified by quanTIseq analysis in a human LUAD cohort (Data generated from
1006 TIMER2.0). R, Spearman correlation. (E) Flow cytometric analysis of parental or REEP2-depleted
1007 (REEP2 KO #25 or #44) 344SQ-generated flank tumors isolated from syngeneic,
1008 immunocompetent mice (n = 10 tumors per cohort). Percentages of T cells ($CD8^+$ T cells,
1009 $CD44^{high}/CD62L^{high}$ naïve $CD8^+$ T cells, $PD1^+/TIM3^+$ exhausted $CD8^+$ T cells and $CD25^+/FOXP3^+$
1010 $CD4^+$ Treg cells), MDSCs, and antigen-presenting cells (total macrophages, M1 macrophages,
1011 and M2 macrophages) were quantified. (F) Flank tumor volume (left) and weight (right) in
1012 syngeneic, immunocompetent mice (dots) injected with parental or REEP2-depleted (REEP2 KO
1013 #25 or #44) 344SQ cells. (G) Schematic illustration of a working model. ZEB1 relieves REEP2
1014 from miR-183- and miR-193a-mediated silencing, thereby locating ERES on the Golgi and
1015 facilitating pro-metastatic secretion that recruits MDSC in the TME and promotes cancer
1016 progression.
1017
1018

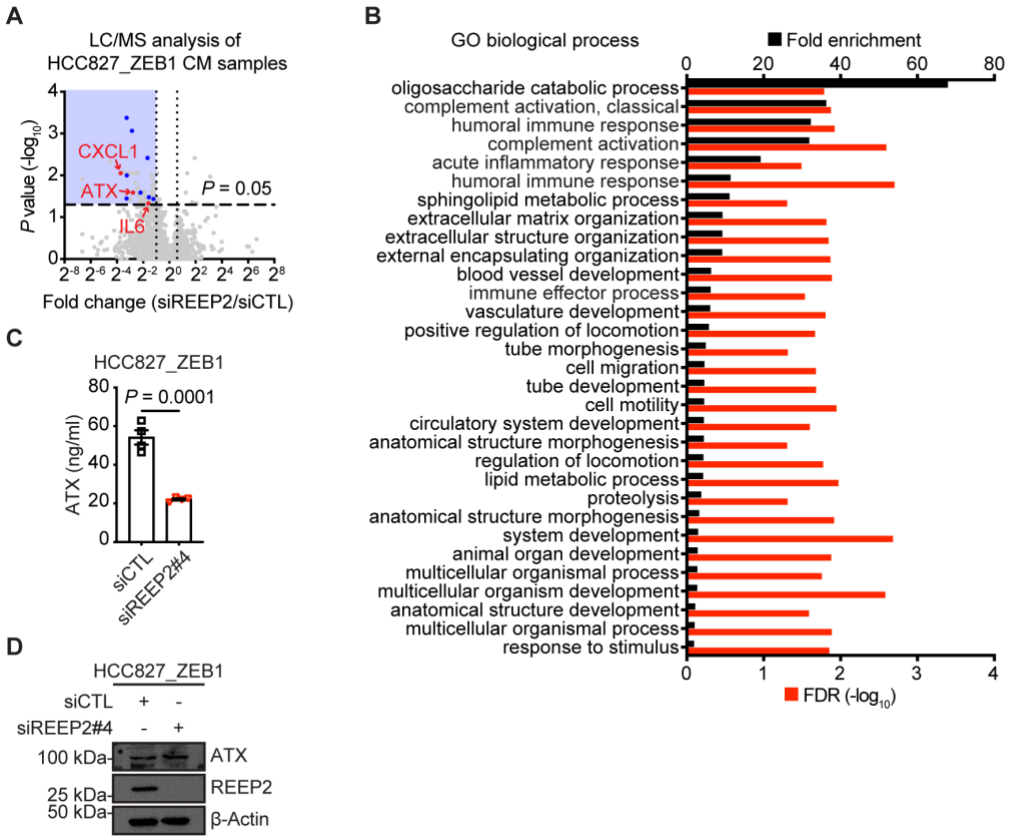

Figure S6. REEP2 activates a pro-metastatic secretion. (A) Volcano plot of proteins identified by LC/MS analysis of CM samples. *P* values (Y axis) and fold-change (X axis). Blue box indicates proteins with significantly reduced secretion (blue box, $P < 0.05$) in REEP2-depleted HCC827_ZEB1 cells (siREEP2). The blue and red dots label the factors that are associated with immune regulation. (B) Enrichment analysis (Fisher's exact test using Gene Ontology terms) of the down-regulated secreted proteins. (C) ELISA assay shows the ATX levels in CM samples (n = 4 replicates per group). *P* values were determined using two-tailed Student's t-test. (D) WB analysis of ATX and REEP2 levels in human HCC827_ZEB1 cells transfected with control siRNA (siCTL) or REEP2 siRNA (siREEP2#4). β-actin loading control.